

# Structural evolution in photodeposited nickel (oxy)hydroxide oxygen evolution electrocatalysts

Martin A.W. Schoen,<sup>†</sup> Nicholas M. Randell,<sup>†</sup> Oliver Calderon,<sup>†</sup> Santiago Jimenez  
Villegas,<sup>†</sup> Zachary Thomson,<sup>†</sup> Roman Chernikov,<sup>‡</sup> and Simon Trudel<sup>\*,†</sup>

<sup>†</sup>*Department of Chemistry and Institute for Quantum Science and Technology, University of  
Calgary, 2500 University Dr NW, Calgary, AB T2N 1N4 Canada*

<sup>‡</sup>*BIOXAS Beamline, Canadian Light Source, 44 Innovation Boulevard, Saskatoon, SK, S7N 2V3,  
Canada*

E-mail: [trudels@ucalgary.ca](mailto:trudels@ucalgary.ca)

## Abstract

Amorphous metal oxides expand the range of material parameters significantly compared to their crystalline counter parts. However, predictions of the exact nature of the amorphous phase and its effect on material properties are still elusive. Thorough structure-property investigations of well-known model systems are thus necessary before predictive control of useful material properties is obtained. In this work, we fabricate a series of photodeposited nickel (oxy)hydroxide ( $\text{NiO}_x$ ) thin films and anneal them at temperatures up to 1000 °C. EXAFS, XRD and XPS are used to determine the local structure, allowing us to correlate it to measured electrochemical properties. We find an amorphous  $\text{Ni}(\text{OH})_2$ -like local structure for annealing conducted below 250 °C, followed by an amorphous-to-amorphous phase transition to a NiO-like structure by 300 °C, thus supplying evidence for different

amorphous polymorphs in this Ni-O system. Above 400 °C a cubic NiO XRD diffraction pattern is detected. Electrochemically, we find a stepwise increase of the onset overpotential at this transition, indicating a change in potential-determining step and possibly OER reaction mechanism. The Tafel slope decreases linearly with annealing temperature, which we attribute to a decrease in (Ni)OOH reaction intermediary coverage, supported by *in-operando* UV-Vis electrochromism. Furthermore, we find that the (Ni)OOH coordination is increasingly strained with annealing temperature, which manifests in higher electrochromic coloring rates and lower binding energies. We identify this as the root cause of the lowered intermediary coverage. Thus, nano-crystalline NiO should kinetically be a superior catalyst to amorphous Ni(OH)<sub>2</sub>. However, at our benchmarking value of 10 mA cm<sup>-2</sup> the amorphous material exhibits lower overpotential, due to a combination of lower onset potential, large chemically active surface area and mass transport limitations under our conditions.

## Introduction

With many countries enacting climate change policies,<sup>1</sup> novel technologies for improved energy efficiency, storage and conversion are required and need to be implemented to achieve the necessary changes in our energy landscape. For many of those new technologies, widespread implementation hinges on targeted development of engineered materials to improve performance, efficiency, and cost. Metal oxides provides opportunity for such an approach and have been investigated for many applications, such as catalysis,<sup>2</sup> active materials in solar cells,<sup>3</sup> batteries,<sup>4,5</sup> electrochromic applications,<sup>6</sup> and (pseudo-)capacitors.<sup>7</sup>

Crystalline (or poly-crystalline) metal oxides have traditionally been utilized. In recent years, amorphous metal oxides have further increased the range of material properties, which in some cases surpass their crystalline counterparts in performance.<sup>8-10</sup> These amorphous metal oxides (*a*-MOs) are attractive for application because of their economical and scalable fabrication. However, the exact nature of the amorphous phase and how it influences material properties, is still largely unknown.<sup>11</sup> While material properties exploiting increased surface area obviously

benefit from a reduction in crystallite size, the effect on other properties is less straightforward. The general description of an amorphous material is that it lacks the translational symmetry of crystalline materials; experimentally, materials are designated as (XRD-)amorphous if they do not exhibit detectable XRD diffraction patterns. This often leads to their depiction as disordered crystals; however, random atomic arrangement is a more fitting definition.<sup>11</sup> Yet, a close-range order persists in amorphous metal oxides, often only extending to the first or second coordination shells, and possibly extending up to the third or fourth coordination shells. Despite this close-range order, these materials are all classified as XRD-amorphous, with no further distinction. This lack of strict definition already illustrates the difficulty of theoretical description of the amorphous phase, as it in itself is not clearly defined. Thus, it has been experimentally observed that amorphous materials can exhibit enhanced vacancy concentrations,<sup>12</sup> altered coordination environments,<sup>13</sup> or strain<sup>14</sup> compared to crystalline, or nano-crystalline counterparts. However, a prediction of these effects is non-trivial and remains elusive.

Therefore, studies on model systems correlating local structure to macroscopic properties are necessary to advance our understanding of amorphous materials. Nickel oxides in their crystalline forms have been intensely studied as catalysts, battery contact materials, or electrochromic materials and thus are a good model system to investigate in the amorphous state.<sup>15</sup> We have used photochemical deposition to readily achieve amorphous metal oxide thin films,<sup>16,17</sup> including nickel (oxy)hydroxides.<sup>8,18</sup> In this work, we anneal a series of photodeposited amorphous  $\text{NiO}_x$ <sup>a</sup> thin films, investigate their structural properties with x-ray absorption, x-ray diffraction, and x-ray photoelectron spectroscopy, and interpret these results in light of their electrochemical and electrochromic properties. This approach allows us to incrementally increase atomic coordination and crystallinity, while observing the changes in material properties. Our main findings are that the  $\text{NiO}_x$  samples are XRD-amorphous below an annealing temperature  $T_{\text{anneal}}$  of 400 °C with an amorphous-to-amorphous coordination transition from  $\text{Ni}(\text{OH})_2$  coordination to  $\text{NiO}$  coordination at  $T_{\text{anneal}} = 250^\circ\text{C}$ , coinciding with a stepwise

---

<sup>a</sup>For the sake of simplicity, throughout this report " $\text{NiO}_x$ " broadly represents a continuum of nickel (oxy)hydroxides, with no implied oxidation state of the nickel centre.

increase in the oxygen evolution reaction (OER) onset potential. We speculate that this step-wise increase in onset potential is caused by a change in OER reaction mechanism. Our electrochromic measurements reveal a decrease of (Ni)OOH reaction intermediary coverage at catalytic onset with increasing  $T_{\text{anneal}}$ , as well as an increase in coloration rate above the coordination transition, eluding to a lower OOH binding energy. We assume an increasing strain in the (Ni)OOH coordination, as observed by EXAFS, as the root cause of this behavior. Electrochemical measurements show an approximately linearly decreasing Tafel slope with  $T_{\text{anneal}}$ , which we, in the light of our observations of the OOH coverage, attribute not to a change in rate determining step, but to the decrease in OOH coverage with  $T_{\text{anneal}}$ . Under our measurement conditions, benchmarking of the catalysts at  $10 \text{ mA cm}^{-2}$  has the amorphous  $\text{Ni}(\text{OH})_2$  catalyst in the lead, despite the superior kinetics exhibited by the nano-crystalline NiO catalyst.

## Results

Amorphous  $\text{NiO}_x$  thin films were prepared using photochemical deposition as previously reported.<sup>8,18,19</sup> These films were used as-prepared (**Ni-AP**) or annealed in air at various temperatures (**Ni-XXX**, where "XXX" is the annealing temperature). Sample preparation and full experimental details are provided in the Supporting Information.

## XRD

The XRD patterns of the  $\text{NiO}_x$  thin films do not show any diffraction peaks at  $T_{\text{anneal}}$  below  $400 \text{ }^\circ\text{C}$  (Fig. 1a). For higher  $T_{\text{anneal}}$  the NiO(111) peak gradually begins to show; however the NiO(200) peak only becomes visible for the **Ni-1000** sample. All diffraction peaks are significantly broadened in comparison to the signal of a crystalline sample. We assume that this broadening is mostly due to small crystallite size in our samples, which we estimate using the Scherrer equation (Eq. S1). The determined crystallite size  $d_{\text{cr}}$  is plotted in Fig. 1b. A clear increase in  $d_{\text{cr}}$  with annealing temperature is observed, indicating that the sample is nanocryst-

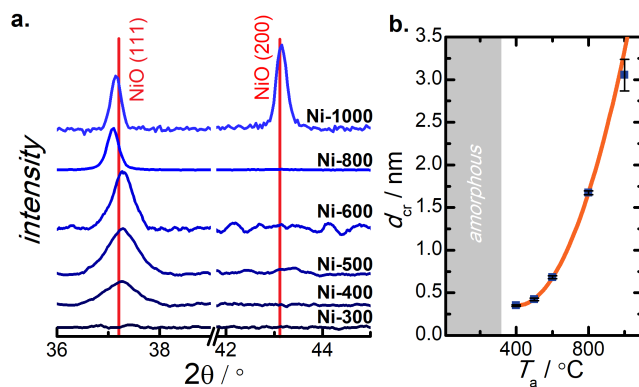


Figure 1: Structural characterization via XRD. a. XRD patterns for  $\text{NiO}_x$  thin films annealed at various temperatures indicate samples are x-ray amorphous up to a  $T_{\text{anneal}}$  of 300 °C. b. For crystalline samples, the grain size was determined by the Scherrer equation, showing crystallite sizes increase with  $T_{\text{anneal}}$ , following a qualitative quadratic trend (solid line).

talline above  $T_{\text{anneal}}$  of 400 °C and that crystallites further grow after initial nucleation of sub-nm crystalline domains. Qualitatively,  $d_{\text{cr}}$  increases quadratically with  $T_{\text{anneal}}$ . A similar increase of  $d_{\text{cr}}$  with annealing temperature has been observed for nickel oxides<sup>20</sup> and a multitude of other materials.<sup>21–23</sup>

## XPS

The Ni  $2p_{3/2}$  XPS spectra of a subset of samples are plotted in Fig. 2a; all fit parameters are reported in Tables S1 and S2. Qualitatively, the **Ni-AP** spectrum is well reproduced by features associated with  $\text{Ni}(\text{OH})_2$  (green lines), while the **Ni-600** sample predominantly exhibits peaks associated with NiO (blue lines). For intermediate  $T_{\text{anneal}}$ , samples show peaks characteristic of both NiO and  $\text{Ni}(\text{OH})_2$ , a representative example being **Ni-250** in Fig. 2a. To achieve a best fit, a low-percentage contribution of NiOOH peaks needs to be included (gray lines). With the characteristic peaks of these three compounds, a good overall fit (red lines) is obtained for all samples. The resulting speciation is plotted against  $T_{\text{anneal}}$  in Fig. 2b. These results back up the qualitative observations and show that **Ni-AP** largely consists of  $\text{Ni}(\text{OH})_2$  (94 %). With increasing  $T_{\text{anneal}}$  the NiO concentration increases at the expense of the  $\text{Ni}(\text{OH})_2$  concentration. Already, **Ni-300** consists of 90 % NiO and for **Ni-600** the NiO content increases to 95 %. All sam-

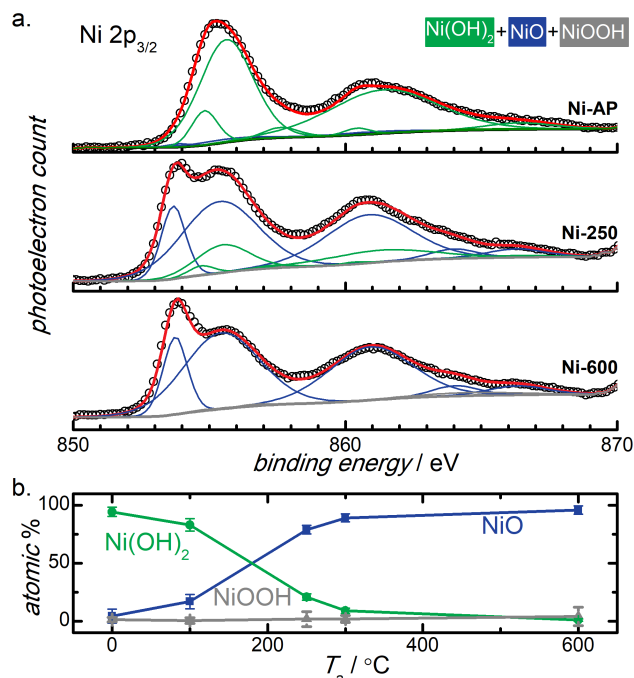


Figure 2: Ni 2p<sub>3/2</sub> X-ray photoelectron spectra of selected samples. a. The Ni 2p<sub>3/2</sub> edge XPS signal of NiO<sub>x</sub> samples not annealed (**Ni-AP**), and annealed at 250 and 600 °C (**Ni-250** and **Ni-600**, respectively) were fit (red line) using NiO, Ni(OH)<sub>2</sub>, and NiOOH components (blue, green, and gray lines, respectively). The Shirley background is not plotted for clarity. b. The fitting indicates that as the  $T_{\text{anneal}}$  increases, the concentration of NiO increases at the expense of Ni(OH)<sub>2</sub>, while the contribution from NiOOH remains largely unchanged.

ples consist of 2-5 % of NiOOH, with no discernible trend with  $T_{\text{anneal}}$ . O 1s XPS spectra, as shown in Fig. S2, qualitatively support these observations.

## X-ray absorption spectroscopy

### XANES

XANES spectra of annealed and *post operando* (**PO**, see SI) samples – along with reference compounds Ni(OH)<sub>2</sub> and NiO – are plotted in Fig. S3. Qualitatively, samples **Ni-AP** to **Ni-230** resemble the Ni(OH)<sub>2</sub> spectrum, while samples **Ni-250** to **Ni-600** more closely match the NiO reference. While the **PO** spectra match the annealed samples at temperatures above 300 °C, they deviate significantly for lower annealing temperatures. All samples exhibit a small pre-edge feature and the sample's oxidation state can be determined from the energy difference

between pre-edge feature position and edge position.<sup>24</sup> The resulting oxidation states are plotted in Fig. S3b. Samples **Ni-AP** through **Ni-600** exhibit a  $T_{\text{anneal}}$  independent oxidation state of approximately +2, while **Ni-AP-PO** has an oxidation state of approximately +2.5 which smoothly decreases with  $T_{\text{anneal}}$  to +2 by **Ni-400-PO**.

## EXAFS

The Fourier transform of the EXAFS signal is plotted in Fig. 3a for selected samples (the complete data set can be found in Fig. S4) and the NiO standard for comparison. Qualitatively, the EXAFS signal below a  $T_{\text{anneal}}$  of 250 °C shows only a small amplitude, as well as little to no ordering beyond the first two coordination shells – associated with coordinating oxygen ions, and nearest neighbour Ni atoms, respectively. This lack of features at higher  $R$  indicate that only a loose close-range order persists, which is consistent with XRD results presented above. At higher annealing temperatures, the second coordination shell peaks becomes larger than the oxygen shell, and other peaks appear at larger  $R$ . A further change in the spectra occurs between 300 and 600 °C, where the peaks found at  $R > 3$  Å increase in amplitude, as well as in sharpness.

Modeling of the first two shells yields the coordination number  $N$ , Ni-O and Ni-Ni bond distances, and Debye-Waller factors  $\sigma^2(\text{O})$  and  $\sigma^2(\text{Ni})$ , see Fig. 3b-d and Table S3. Due to a large uncertainty in the fit, higher shells are not modeled. For all samples annealed up to a  $T_{\text{anneal}}$  of 250 °C the coordination number  $N$  is constant at a value of approximately 4.5, which increases to a value of approximately 6 when annealed above 300 °C (Fig. 3b). The determined Ni-O and Ni-Ni bond distances are presented in Fig. 3c and d, respectively. For samples **Ni-AP** through **Ni-225**, the Ni-O bond distance is approximately 2.04 Å, which is indicative of a  $\alpha$ -Ni(OH)<sub>2</sub> coordination<sup>25,26</sup> (lower dashed line). At  $T_{\text{anneal}} = 250$  °C, the Ni-O bond distance increases in a stepwise fashion to approximately 2.075 Å, close to the value 2.07 Å for bulk NiO (upper dashed line).<sup>25</sup> Similarly, the Ni-Ni bond distance decreases from 3.075 Å (bulk  $\alpha$ -Ni(OH)<sub>2</sub> = 3.08 Å<sup>26</sup>) at low  $T_{\text{anneal}}$  stepwise to 2.96 Å (bulk NiO = 2.94 Å<sup>26</sup>) at larger  $T_{\text{anneal}}$ . The Debye-Waller factors

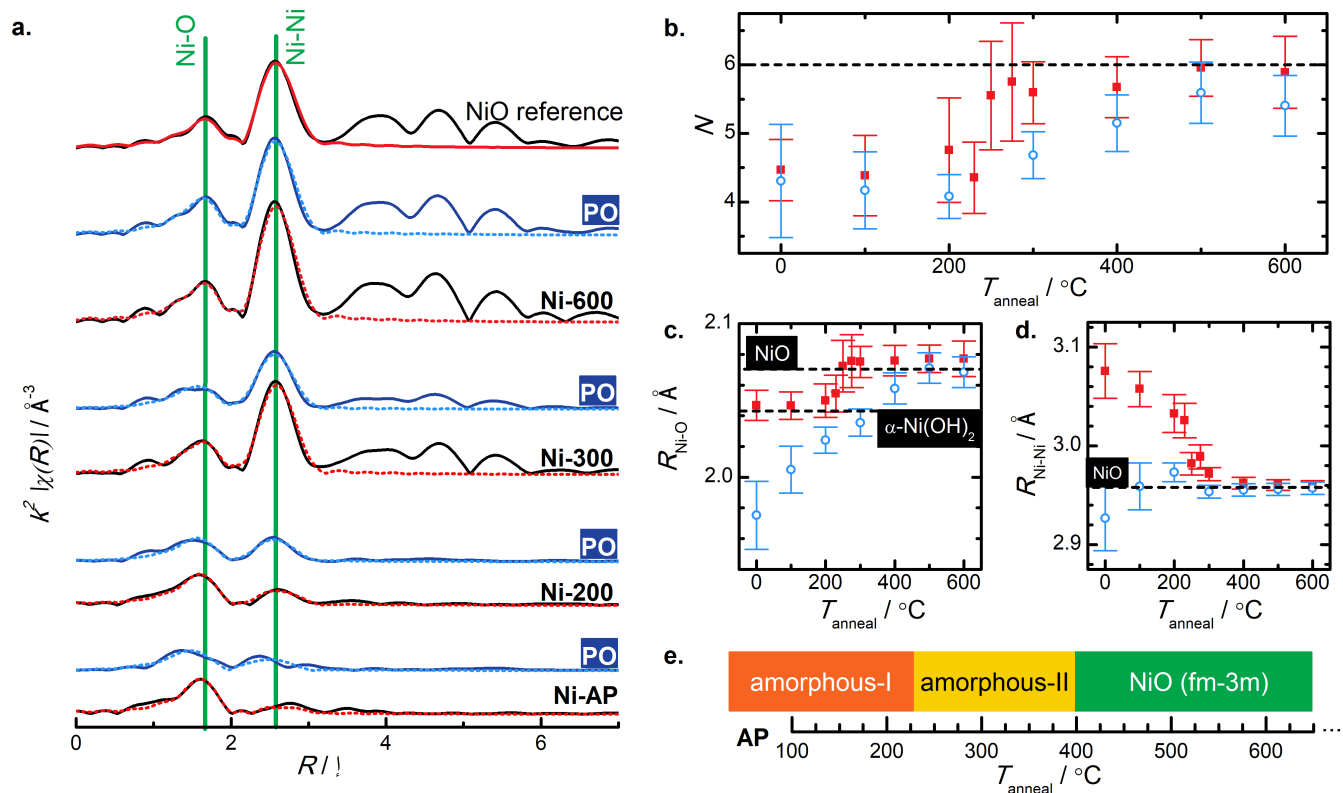


Figure 3: a. The  $k^2$  weighted Fourier transform of the EXAFS signal is plotted for select samples. Black lines are annealed samples, with red lines being the NiO model of the first two shells. Blue lines represent samples from the *post operando* electrochemically treated series (PO), with light blue lines representing the first two shell model. In b.-d. the modeled EXAFS parameters are plotted against  $T_{\text{anneal}}$ , which show the coordination number  $N$ , oxygen bond distance, and Ni bond distance, respectively. Red filled squares represent the annealed series, blue open circles the annealed and then electrochemically treated series, and dashed lines the NiO reference values. In c. the bond distance  $\alpha\text{-Ni(OH)}_2$  is additionally plotted as a dashed line. e. Shows a schematic of the sample structure with  $T_{\text{anneal}}$ .

$\sigma^2$  drop stepwise at  $T_{\text{anneal}} = 250$  °C for both the oxygen and nickel paths (Table S3).

The EXAFS spectra of electrochemically treated samples ( $j = 15$  mA cm<sup>-2</sup>, 2 min) were recorded *post operando* (labelled **PO** and plotted in blue in Fig. 3). Qualitatively, the **PO** samples behave similarly to the annealed series, however they generally exhibit a smaller amplitude, as well as a shift in peak position at low annealing temperatures. The Ni-O bond distance for the **PO** samples is lower for all samples and increases almost linearly with  $T_{\text{anneal}}$  from 1.975 Å at 100 °C to 2.07 Å at 500 °C. The Ni-Ni bond distance of the electrochemically treated samples stays – within errors – constant with  $T_{\text{anneal}}$ .  $\sigma^2(\text{O})$  of the **PO** samples stay, within errors, constant with  $T_{\text{anneal}}$ , while  $\sigma^2(\text{Ni})$  mirrors the step decreases at  $T_{\text{anneal}} = 250$  °C. All parameters converge to the NiO reference sample values with increasing  $T_{\text{anneal}}$ . Fit parameters are collated in Table S3.

The contraction of the Ni-O bond distances with increasing oxidation state in nickel oxides offers another method to determine oxidation state.<sup>27</sup> Results for the **PO** sample series are plotted in Fig. S3b and match within errors the oxidation numbers determined from XANES in the previous section.

## Electrochemical properties

### Electrochemistry

Measured cyclic voltamograms (CVs) and step voltammetry can be found in Figs. S5-S7. The extracted Tafel slopes are plotted in Fig. 4a against  $T_{\text{anneal}}$ . A linear guide to the eye is superimposed, to illustrate the steady decrease of the Tafel slope with  $T_{\text{anneal}}$ . The overpotentials  $\eta$  at catalytic onset and at  $j = 10$  mA cm<sup>-2</sup> behave rather differently than the Tafel slope, and increase in a single step around  $T_{\text{anneal}} = 250$  °C. The Tafel slope values are in the range of previously reported values of similar NiO<sub>x</sub> films<sup>18</sup> and are lower than values for crystalline NiO<sup>28</sup> (not corrected for Fe electrolyte impurities), or NiO<sub>x</sub> nanoparticles.<sup>29</sup> Both  $\eta$  at onset and at  $j = 10$  mA cm<sup>-2</sup> exhibit values close to previously reported ones.<sup>18,30,31</sup>

The double-layer capacitance  $C_{\text{dl}}$  (estimated from sweep-rate dependent CVs in the non-

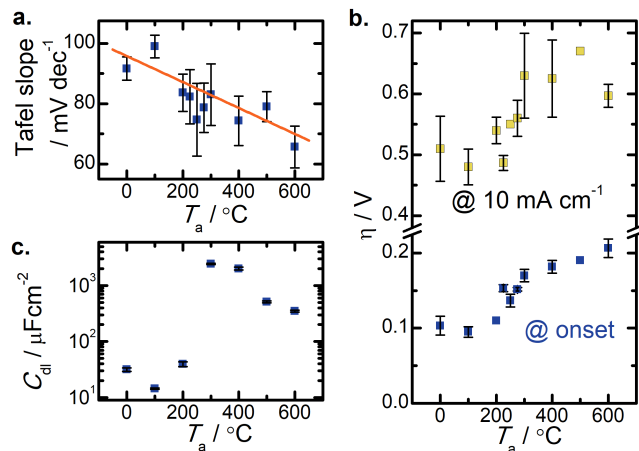


Figure 4: Electrochemical properties as a function of  $T_{\text{anneal}}$ . a. the Tafel slope with line as guide to the eye, b. the over-potential  $\eta$  at onset and  $j = 10 \text{ mA cm}^{-2}$ , and c. the double-layer capacitance  $C_{\text{dl}}$ .

Faradaic range, Fig. S8) exhibits values in the  $\mu\text{F}$  range for  $T_{\text{anneal}}$  below 300 °C (Fig. 4c). It increases 75-fold for **Ni-300** compared to **Ni-AP**. A similar (22-fold) increase in double-layer capacitance  $C_{\text{dl}}$  at  $T_{\text{anneal}} = 300 \text{ °C}$  has been reported for electrochemically deposited  $\text{Ni}(\text{OH})_2$  films and attributed to a simultaneous increase in both the active surface area, and the specific capacity, the latter being the predominant factor.<sup>32</sup> For higher  $T_{\text{anneal}}$   $C_{\text{dl}}$  decreases again almost linearly, which we attribute to the increase in  $d_{\text{cr}}$  and the resulting decrease in the active surface area.

The position of the oxidation peak of the Ni redox couple ( $E_{\text{p,a}}$ , determined in the up sweep at a sweep rate of 0.01 V/s) shifts approximately linearly with  $T_{\text{anneal}}$  from 1.34 V vs RHE for **Ni-AP** to 1.28 V vs RHE for **Ni-600** (CVs are in Fig. S5). Comparing the position of this peak in the first CV to the position in a steady-state CV, we observe a shift of approximately 0.04 V for all samples. The shift is reversed on the back sweep. This behavior differs from what was previously observed in  $\text{Ni}(\text{OH})_2$  films<sup>33</sup> where an up-sweep shift in the opposite direction and no down-sweep shift were observed.

It was observed that samples that were initially clear and transparent colored to a dark blue-grey hue when subjected to an applied potential, indicating the samples are electrochromic, as

has been previously reported for  $\text{NiO}_x$ .<sup>34-36</sup> In light of this, we took advantage of this property to further investigate the samples, as is laid out in the next section.

## Electrochromism

The electrochromic effect in nickel oxides is attributed to the transition of  $\text{Ni}^{2+}$  to a higher oxidation state of  $\text{Ni}^{3+}$  or  $\text{Ni}^{4+}$ , *i.e.* from  $\text{NiO}$  or  $\text{Ni(OH)}_2$  to  $\text{NiOOH}$  or  $\text{NiOO}$ .<sup>35</sup> Simultaneously, almost all proposed OER mechanisms involve the formation of  $\text{NiOOH}$  or  $\text{NiOO}$  as a reaction intermediary, for example via hydro-peroxide,<sup>37</sup> electrochemical metal peroxide,<sup>38</sup> or lattice oxygen.<sup>39</sup> Thus, the  $\text{Ni-OH (NiO)} \rightarrow \text{Ni-OOH/Ni-OO}$  reaction step(s) can be directly probed by monitoring the electrochromic response to an applied potential and the population (coverage) of the  $\text{Ni}^{3+}$  species is proportional to the coloring of the film. The steady-state spectra under various conditions are presented in the SI (Figs. S9 and S10).

**Coloration kinetics.** Electrochromic kinetics are measured by applying a potential and tracking transmission at a given wavelength ( $\lambda = 450$  nm in this case) over time, as shown in Fig. 5 for samples **Ni-100**, **Ni-300**, and **Ni-600**. Three different potential steps ( $E_{p,a}$ , 1.9 V vs RHE, and 2.4 V vs RHE) are applied at  $t = 0$  s. With  $E_{p,a}$  potential applied the transmission drops and then stays constant. This coloring decreases with  $T_{\text{anneal}}$  from  $\approx 25\%$  transmission for **Ni-100** and  $\approx 50\%$  transmission for **Ni-300** to only  $\approx 85\%$  transmission for **Ni-600**. At higher potentials all samples exhibit an initial fast coloring step to approximately the respective  $E_{p,a}$  coloring level, followed by slower further coloring of the samples. This additional coloring takes up to 75 s to stabilize at 1.9 V applied potential or 30 s at 2.4 V. All samples color to roughly the same level at 1.9 V or 2.4 V.

The initial coloration is fit with an exponential decay of transmission for all samples (left panels in Fig. 5). When  $E_{p,a}$  is applied the coloring perfectly follows the exponential decay function, while for higher potentials, the coloring occurs faster than modeled with a single exponential decay, indicating a second process must be occurring. The extracted coloring rates ( $r$ ) are plot-

ted against  $T_{\text{anneal}}$  in Fig. 5d and listed in Table S4. For all applied potentials, the coloring rates decrease with  $T_{\text{anneal}}$  to a minimum at  $T_{\text{anneal}} = 250$  °C; from there the rates increase steadily with  $T_{\text{anneal}}$ . Coloring rates with higher applied potentials (1.9 V or 2.4 V vs. RHE) are approximately an order or magnitude larger than the rates with  $E_{p,a}$  applied. The arrows in respective colors mark the time where the applied potential is switched off. When the  $E_{p,a}$  potential was applied, the transmission remains constant upon removing this potential. For the two higher potentials, the colored state partially bleaches to  $E_{p,a}$  level once the potential is set to open current potential.

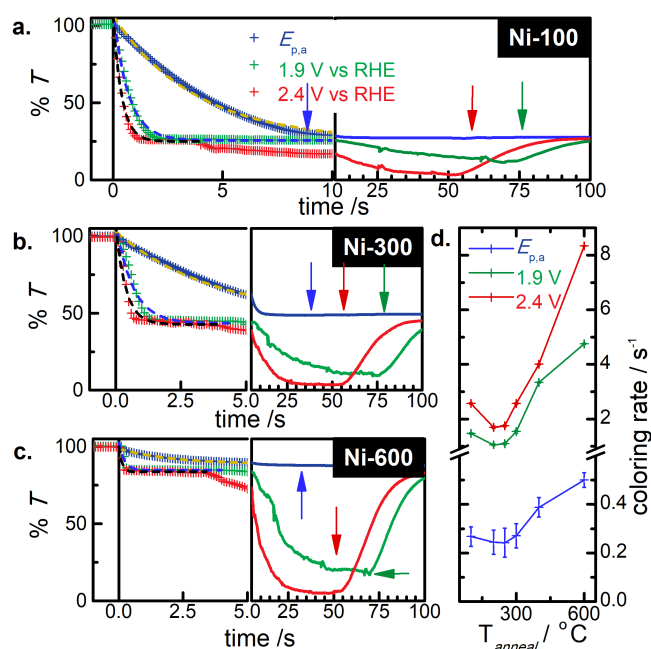


Figure 5: Transmission at  $\lambda = 450$  nm plotted against measurement time. 100 % transmission is defined at OCP before applying potential. A potential of pre-oxidation peak value  $E_{p,a}$  (blue symbols and lines), 1.9 V vs RHE (green symbols and lines), and c. 2.4 V vs RHE (red symbols and lines) is applied at  $t=0$  s for samples annealed at a. 100 °C, b. 300 °C, and c. 600 °C. The respectively colored arrows signify the time the potential is turned off. Dotted lines are exponential decay fits to the initial coloring step and resulting coloring rates are plotted in d.

**CV tracking.** The electrochromic response of NiO<sub>x</sub> thin films corresponds to a change in chemical state,<sup>35</sup> thus the chemical state of a catalyst can be deduced from a direct comparison between cyclic voltammetry and electrochromism by measuring the *in situ* UV-vis transmission

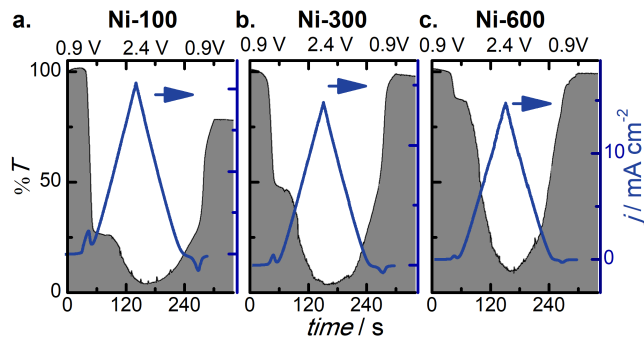


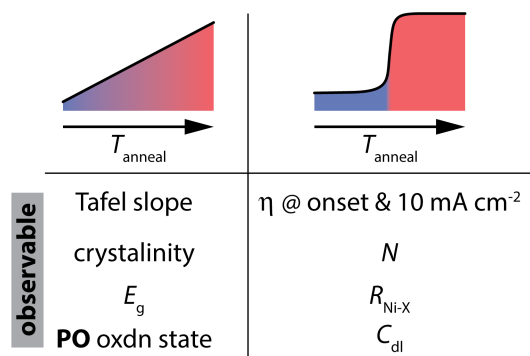
Figure 6: Transmission at  $\lambda = 450$  nm plotted against time (black lines and grey area, lhs and bottom axis) and current density plotted against applied RHE potential (blue lines, rhs and top axis) for samples annealed at a. 100 °C, b. 300 °C, and c. 600 °C during single CV at 0.01 V/s.

at a fixed wavelength ( $\lambda = 450$  nm) in an electrochemical cell, while simultaneously performing CV measurements. The results for samples **Ni-100**, **Ni-300**, and **Ni-600** are plotted in Figs. 6 and S11 for sweep rates  $\nu = 0.01$  V s<sup>-1</sup> and  $\nu = 0.1$  V s<sup>-1</sup>, respectively.

At the slower sweep rate ( $\nu = 0.01$  V s<sup>-1</sup>, Fig. 6) the transmission of **Ni-100** abruptly drops at  $E_{p,a}$  to  $\approx 25\%$ . At approximately 1.8 V vs. RHE an additional slower coloring occurs to sub-10% transmission at 2.4 V. On the reverse sweep this behavior reverses and a delayed slow bleaching occurs until  $E_{p,c}$  whereupon fast bleaching partially recovers transmission. The transmission CV tracking for **Ni-300** and **Ni-600** is similar to the **Ni-100** sample, however initial coloring only proceeds to 50 % and 85 % transmission respectively, and the additional coloring occurs at lower potentials of 1.65 V for Ni-300 and 1.55 V for Ni-600. For **Ni-300** and **Ni-600** the transmission is fully recovered upon cycling.

## Discussion

The measured observables can be split up into two groups depending on their behavior with  $T_{\text{anneal}}$ , compare Scheme 1. One group changes continuously with  $T_{\text{anneal}}$ , while the other changes abruptly in a stepwise fashion (Scheme 1). The diffractograms in Fig. 1 clearly show that samples are XRD-amorphous for  $T_{\text{anneal}}$  below 400 °C. However, EXAFS measurements provide further insight in the local structure of those samples. At low annealing temperatures no



Scheme 1: List of observables and behavior with  $T_{\text{anneal}}$

long-range order persists, as seen by the lack of peaks in the Fourier transform of the EXAFS signal at high  $R$  (see Fig. 3a). Above  $T_{\text{anneal}} = 200$  °C, further peaks appear gradually, indicating an increase in coordination for neighbours beyond the first and second coordination shells. It is noteworthy that at this point the samples are still XRD-amorphous, and therefore the increase in coordination means that there are several phases of amorphous  $\text{NiO}_x$  with different coherence lengths. At  $T_{\text{anneal}} = 400$  °C XRD diffraction peaks are detected as the material crystallizes to NiO. Crystallite sizes can be determined to increase continuously and approximately quadratically with further annealing. Thus, we conclude that above an activation temperature of approximately 200 °C the coordination and crystallinity increases continuously in the  $\text{NiO}_x$  films. It is worth noting that all the amorphous instances are not identical, providing a rich structural space with several polymorphs, an example of polyamorphism.<sup>40,41</sup>

The bond distances of the annealed samples are consistent with a  $\text{Ni}(\text{OH})_2$  coordination environment, most likely  $\alpha$ - $\text{Ni}(\text{OH})_2$ . This is corroborated by XPS results, which establish that the surface (*ca.* top 5 nm) of samples annealed below 250 °C largely consists of  $\text{Ni}(\text{OH})_2$ . While XPS is not representative of the whole sample, combining it with more depth-penetrating EXAFS results allows us to draw conclusions on the whole sample. EXAFS yields a coordination number of approximately 4.5 for the  $\text{Ni}(\text{OH})_2$  phase, which is nominally 6-fold coordinated. However, electrochemically deposited  $\text{Ni}(\text{OH})_2$  has been shown to exhibit H-substituted nickel vacancies<sup>32</sup> and associated oxygen vacancies at a concentration of approximately 33 %. H atoms contribute a negligible signal in EXAFS due to their low scattering cross section. Thus, within errors

our under-coordinated  $N$  matches the previously reported vacancy concentration. We note that these under-coordinated Ni sites may act as active OER sites, contributing to the higher activity of the amorphous samples (*vide infra*).

The contraction (extension) of the Ni-Ni (Ni-O) bonds between **Ni-200** and **Ni-275** is consistent with a transition from Ni(OH)<sub>2</sub> to NiO.  $N$  similarly changes in a single step from under-coordinated to fully coordinate octahedral, as expected for NiO.<sup>42</sup> XPS for **Ni-300** and **Ni-600** confirm that our samples mostly transitioned to NiO, which is confirmed by XRD for samples annealed above 400 °C, once the crystallite size grows above the detection limit. Oxidation states, deduced from XANES edge position and Ni-O bond distance, scatter within error around +2 for samples **Ni-AP** to **Ni-600**, as expected for both Ni(OH)<sub>2</sub> and NiO. A phase transition from Ni(OH)<sub>2</sub> to NiO has been reported for samples produced under a variety of conditions.<sup>43,44</sup> In our sample series the Ni(OH)<sub>2</sub>-to-NiO phase transition occurs as an amorphous-to-amorphous transition, allowing us to directly compare Ni sites in amorphous Ni(OH)<sub>2</sub> and NiO coordination environments. Furthermore, this phase transition explains the stepwise behavior of bond distances and coordination number with  $T_{\text{anneal}}$ .

The **PO** samples exhibit the same sharp transition of coordination number, however they do not show the sharp transition of bond distances. At low  $T_{\text{anneal}}$  the Ni-O distances are significantly lower and increase smoothly with  $T_{\text{anneal}}$ . Shorter bond distances usually indicate a higher oxidation state and allow deduction of the oxidation state.<sup>27</sup> Thus, we determine an average oxidation state of +2.6 for **Ni-AP-PO**, which linearly decreases to +2 for **Ni-400-PO**, which is confirmed by XANES edge positions (*c.f.* Fig. S3). Shorter bond distances and increased oxidation state are indicative of a NiOOH-like coordination, which has oxidation states of Ni<sup>3+</sup> (and Ni<sup>4+</sup> in the  $\gamma$  phase) and O-bond distances of 1.934 Å for  $\beta$ -NiOOH and 1.882 Å for  $\gamma$ -NiOOH.<sup>25</sup> Bond distances in the **PO** NiOOH coordination are larger than in crystalline samples, indicating a strained coordination. The existence of NiOOH in the **PO** series is expected, since Ni<sup>3+</sup> or Ni<sup>4+</sup> have been identified as the catalytically active species.<sup>45</sup> Therefore, we identify this transition in the **PO** series as a strained NiOOH/Ni(OH)<sub>2</sub> to NiO amorphous-to-amorphous phase transi-

tion.

As a side note, the coordination number of the **PO** series may be – although not conclusively outside of error bars – lower than the annealed series for all samples. This could indicate that some amount of Ni is dissolved in the electrolyte solution, creating Ni vacancies as previously suggested.<sup>46</sup> A rough estimate, averaged over all samples, suggests that approximately 10 % Ni is dissolved by the electrochemical reaction in both the NiOOH/Ni(OH)<sub>2</sub> and NiO **PO** phases.

The NiO<sub>x</sub> catalysts are electrochemically characterized by measuring the Tafel slope, overpotential at catalytic onset  $\eta_{\text{onset}}$ , overpotential  $\eta$  at 10 mA/cm<sup>2</sup>, and double layer capacitance  $C_{\text{dl}}$ . The Tafel slope decreases linearly with  $T_{\text{anneal}}$  while all the other electrochemical descriptors increase stepwise at the Ni(OH)<sub>2</sub>-NiO transition. For the overall efficiency of the OER two reaction steps are relevant.<sup>47</sup> First the rate-determining step (RDS) – the step with the lowest reaction rate, and the potential-determining step (PDS) – the step with the highest activation potential. These two steps can be correlated to the Tafel slope, which provides insight about the RDS and  $\eta_{\text{onset}}$ , which directly corresponds to the magnitude of the activation potential of the PDS.

Several recent reports have identified crystalline strain as a significant influence on catalytic performance.<sup>14,48</sup> While we cannot draw direct conclusions about conditions at catalysis, our **PO** EXAFS results indicate the existence of a strained NiOOH-like environment during catalysis. Debye-Waller factors in this coordination exhibit larger values than the crystalline references, compare Table S3, indicating coexistence of coordinations throughout the sample. The oxygen bond distances increase continuously with  $T_{\text{anneal}}$ , thus increasing the strain in the NiOOH coordination. Kuai *et al.* found a decrease in both Tafel slope and onset potential with introducing strain in a NiOOH catalyst.<sup>48</sup> While we observe opposite behavior in the onset potential, we see a decrease in Tafel slope with increased strain in the **PO** NiOOH coordination.

It is conceivable that the OOH binding energy of the NiOOH coordination depends on the strain in this coordination, *i.e.* the NiOOH coordination is stable and energetically preferred when coordination parameters are close to their crystalline counterparts, but with increasing

strain this coordination becomes energetically less favorable. The effect of lattice strain on adsorption has been theoretically shown in a multitude of systems.<sup>49,50</sup> This directly correlates to the (Ni)OOH OER intermediary coverage, which decreases with decreasing adsorption energy. Our electrochromic measurements allow us to directly probe the NiOOH concentration and we observe a strong decrease of NiOOH concentration (coloring) at catalytic onset with increasing  $T_{\text{anneal}}$ , compare Fig. 6. Thus, we conclude that the NiOOH intermediary coverage decreases with increasing strain. Our determined coloring rates support this argument, insofar as coloring rates increase significantly with  $T_{\text{anneal}}$  above 250 °C indicating faster OOH adsorption and thus, assuming Arrhenius kinetics, a lower binding energy.

A comprehensive study on catalytic materials combining experimental results and kinetic studies was performed by Tao *et al.*<sup>51</sup> This study determines the (Ni)OOH formation as the RDS for a NiOOH catalyst. Shinagawa *et al.*<sup>52</sup> calculated Tafel slopes for OER in relation to intermediate coverage and different RDS, assuming the standard hydro-peroxide mechanism. With the (Ni)OOH formation assumed as the RDS they calculated a Tafel slope of 120 mV dec<sup>-1</sup> for high (Ni)OOH coverage, which is reasonably close to the Tafel slope of samples **Ni-AP** or **Ni-100**, and values previously reported in Fe-free electrolyte.<sup>18</sup> For low (Ni)OOH and high (Ni)O coverage they calculate a Tafel slope of 60 mV dec<sup>-1</sup> which matches closely our determined value for the **Ni-600** sample. These coverages match our electrochromic observations of the NiOOH population at catalytic onset, which is high for **Ni-100** and decreases significantly towards **Ni-600** (see Fig. 6) as well as the mechanism of the stepwise  $C_{\text{dl}}$  increase, which indicates electrochemically stable (persisting without applied potential) NiOOH coverage below  $T_{\text{anneal}} = 250$  °C and electrochemically active coverage above. Thus, we suggest that throughout our sample series the (Ni)OOH formation is the RDS and the continuous change in Tafel slope is the result of a change in NiOOH coverage, caused by strain introduced into the NiOOH coordination.

The stepwise 0.1 V increase in  $\eta_{\text{onset}}$  at the *a*-Ni(OH)<sub>2</sub>-to-*a*-NiO phase transition indicates an increase of the activation potential of the PDS. Li *et al.*<sup>46</sup> calculated the catalytic activity of NiOOH in near-neutral pH conditions. Their findings indicate that the OER proceeds via

a ‘lattice-peroxide’ mechanism in fully coordinated NiOOH, while a ‘hydro-peroxide’ mechanism in 4-fold coordinated NiOOH is operative. A PDS potential difference of 0.3 V (0.32 V) is predicted between the two mechanisms in the the  $\gamma$ -NiOOH ( $\beta$ -NiOOH) phase. Our EXAFS and electrochemical results show coordination numbers  $N$  of approximately 4.5 and  $\eta_{\text{onset}} \approx 0.1$  V for samples **Ni-AP** through **Ni-230** and  $N \approx 6$  and  $\eta_{\text{onset}} \approx 0.2$  V for **Ni-275** through **Ni-600**. Thus, it is conceivable that with the change in coordination environment in our sample series, the OER proceeds via different reaction mechanisms – lattice oxygen for low  $T_{\text{anneal}}$  and hydro-peroxide for high  $T_{\text{anneal}}$ – with a different activation potential. With the similarities in the proposed reaction mechanisms, this does not necessitate a fundamental change of the RDS.

The above mentioned quantities are relevant for determining mechanics of the OER, however for technological application  $\eta$  at  $10 \text{ mA cm}^{-2}$  is a more useful indicator of catalyst performance, as this current density roughly corresponds to the output of a solar cell.<sup>53</sup> In our sample series  $\eta$  at  $10 \text{ mA cm}^{-2}$  increases stepwise by 0.1 V at the Ni(OH)<sub>2</sub>-to-NiO transition, which would indicate that amorphous under-coordinated Ni(OH)<sub>2</sub> catalytically outperforms fully coordinated amorphous NiO or nano-crystalline NiO. However, this is a simplified interpretation. The lower Tafel slope for NiO coordinated samples and the faster electrochromic coloring rates suggest that the reaction rate actually increases with  $T_{\text{anneal}}$ . On the other hand, we find an approximate order of magnitude decrease in chemically active surface area from **Ni-300** to **Ni-600**, which will decrease catalytic efficiency. At the benchmark value of  $10 \text{ mA cm}^{-2}$  mass transport limitations dominate the current density in our measurements (see Fig. S7), thus masking the effects described above and preventing disentanglement of separate contributions to the catalytic activity for the benchmarking value.

Direct tracking of the NiOOH population during CVs (Fig. 6) shows that after initial coloring all samples color further. This additional coloration occurs on a significantly slower time scale than the initial coloring, as shown in Fig. 5, but proceeds to a similar level in all the samples. The latter indicates approximately the same NiOOH concentration in all samples at 2.4 V after 50 s. We assume this to be either the activation of a second catalytic mechanism, possibly the original

hydro-peroxide mechanism exhibited by samples in Ni(OH)<sub>2</sub> coordination, or alternatively the catalytic activation of different Ni sites. The latter, however, only has been observed in (Ni,Fe) oxides.<sup>14</sup> This coloring step is not accompanied by a change in current density, which is not surprising, considering the current is already mass transport limited. **Ni-100** and **Ni-300** also show additional coloring, however for **Ni-100** this is probably due to bubble formation on the sample surface. For **Ni-300** the additional coloring does not occur in a distinct separable step, but we cannot exclude the possibility of it occurring in the initial step, which would explain the slower rates for this sample. While this second mechanism does not play a role for the catalytic efficiency, the knowledge of a second competing mechanism and its activation potential could support theoretical efforts in describing catalytic mechanisms.

## Summary and Conclusion

We produced an annealing series of initially amorphous NiO<sub>x</sub> thin films and find a transition from under-coordinated ( $N \approx 4.5$ ) amorphous Ni in Ni(OH)<sub>2</sub> coordination to fully coordinated amorphous Ni in NiO coordination at approximately  $T_{\text{anneal}} = 250$  °C. This coordination transition leads to a stepwise change in oxygen and nickel bond distances, double layer capacitance and catalytic onset potential. We attribute the step in onset potential to a change in reaction mechanism from a ‘hydro-peroxide’ mechanism to a ‘lattice-oxide’ mechanism, as suggested by theoretical modelling.<sup>46</sup> Furthermore, we observe an increase of ordering length ( $\approx$  crystallinity) to higher coordination shells with  $T_{\text{anneal}}$ , whilst samples are still XRD-amorphous and a continuous increase in crystallite size once XRD detection limit is reached, leading us to conclude that both coordination length and crystallite size change continuously with  $T_{\text{anneal}}$  and that the presented NiO<sub>x</sub> series exhibits several amorphous polymorphs.

The Tafel slope decreases continuously with  $T_{\text{anneal}}$ , caused by a decrease of (Ni)OOH intermediary coverage, as confirmed by electrochromism, rather than a shift in the rate determining step. We attribute the decrease in NiOOH coverage to increased strain in that coordination with

$T_{\text{anneal}}$ , leading to a lower OOH binding energy. Moreover, the Tafel slope data is consistent with calculations determining the (Ni)OOH formation as the rate determining step.<sup>52</sup> Amorphous Ni in Ni(OH)<sub>2</sub> coordination exhibits a lower overpotential at 10 mA cm<sup>-2</sup> than in NiO coordination making it the better catalyst in respect to our benchmarking parameter. However, Tafel slope, electrochromic coloring times, and double layer capacitance indicate that NiO coordinated nano-crystals exhibit faster reaction rates although with lower electrochemical surface area. In our measurements these contributions are masked by mass transport limitations to the current density and disentangling them requires further investigation. In all samples, we observe additional coloring at larger applied potentials, which we attribute to the activation of a second catalytic mechanism, or other catalytically active sites which warrants further investigation pertaining to its exact nature.

## **Acknowledgments**

The authors thank NSERC of Canada (Discovery Grant) for operating funds. This research used facilities funded by the University of Calgary and the Canadian Foundation for Innovation (John R. Evans Leaders Fund). Funding to M.A.W.S. was provided by the Alexander von Humboldt Foundation Feodor Lynen Research Fellowship and the University of Calgary's Global Research Initiative in Sustainable Low Carbon Unconventional Resources funded by the Canada First Research Excellence Fund (CFREF). We thank Emilio Heredia for technical assistance at the BIOXAS beamline. Part or all of the research described in this paper was performed at the Canadian Light Source, a national research facility of the University of Saskatchewan, which is supported by the Canada Foundation for Innovation (CFI), the Natural Sciences and Engineering Research Council (NSERC), the National Research Council (NRC), the Canadian Institutes of Health Research (CIHR), the Government of Saskatchewan, and the University of Saskatchewan.

## Author contributions

MAWS and ST conceived and designed the experiment. MAWS performed electrochemical and electrochromic measurements. MAWS and ZT performed UV-VIS. MAWS, ST, OC, SJ, NR, and RC recorded the XAS spectra. MAWS analyzed the data. MAWS and ST wrote the manuscript; all co-authors provided feedback on the manuscript.

## Conflict of Interest

There are no conflicts of interest to declare.

## References

- (1) REPORT OF THE SECRETARY-GENERAL ON THE 2019 CLIMATE ACTION SUMMIT THE WAY FORWARD IN 2020. *Climate Action Summit 2019*
- (2) Védrine, J. C. Heterogeneous Catalysis on Metal Oxides. *Catalysts* **2017**, 7.
- (3) Wang, J.; Liu, Y.; Chen, X.; Chen, C.; Chen, P.; Wang, Z.; Duan, Y. Functional Metal Oxides in Perovskite Solar Cells. *ChemPhysChem* **2019**, 20, 2580–2586.
- (4) Mattelaer, F.; Geryl, K.; Rampelberg, G.; Dendooven, J.; Detavernier, C. Amorphous and Crystalline Vanadium Oxides as High-Energy and High-Power Cathodes for Three-Dimensional Thin-Film Lithium Ion Batteries. *ACS Appl. Mater. Interfaces* **2017**, 9, 13121–13131.
- (5) Ren, Y.; Chen, K.; Chen, R.; Liu, T.; Zhang, Y.; Nan, C.-W. Oxide Electrolytes for Lithium Batteries. *J Am. Ceram. Soc.* **2015**, 98, 3603–3623.
- (6) Wu, W.; Wang, M.; Ma, J.; Cao, Y.; Deng, Y. Electrochromic Metal Oxides: Recent Progress and Prospect. *Adv. Electron. Mater.* **2018**, 4, 1800185.

- (7) Li, H. B.; Yu, M. H.; Wang, F. X.; Liu, P.; Liang, Y.; Xiao, J.; Wang, C. X.; Tong, Y. X.; Yang, G. W. Amorphous nickel hydroxide nanospheres with ultrahigh capacitance and energy density as electrochemical pseudocapacitor materials. *Nat. Comm.* **2013**, *4*, 1894.
- (8) Smith, R. D. L.; Prévot, M. S.; Fagan, R. D.; Zhang, Z.; Sedach, P. A.; Siu, M. K. J.; Trudel, S.; Berlinguette, C. P. Photochemical Route for Accessing Amorphous Metal Oxide Materials for Water Oxidation Catalysis. *Science* **2013**, *340*, 60–63.
- (9) Yan, S.; Abhilash, K. P.; Tang, L.; Yang, M.; Ma, Y.; Xia, Q.; Guo, Q.; Xia, H. Research Advances of Amorphous Metal Oxides in Electrochemical Energy Storage and Conversion. *Small* **2019**, *15*, 1804371.
- (10) Zhang, C.; Berlinguette, C. P.; Trudel, S. Water oxidation catalysis: an amorphous quaternary Ba-Sr-Co-Fe oxide as a promising electrocatalyst for the oxygen-evolution reaction. *Chem. Commun.* **2016**, *52*, 1513–1516.
- (11) Stachurski, Z. H. On Structure and Properties of Amorphous Materials. *Materials* **2011**, *4*, 1564–1598.
- (12) Yeon, H.-W.; Lim, S.-M.; Jung, J.-K.; Yoo, H.; Lee, Y.-J.; Kang, H.-Y.; Park, Y.-J.; Kim, M.; Joo, Y.-C. Structural-relaxation-driven electron doping of amorphous oxide semiconductors by increasing the concentration of oxygen vacancies in shallow-donor states. *NPG Asia Mat.* **2016**, *8*, e250–e250.
- (13) Triana, C. A.; Araujo, C. M.; Ahuja, R.; Niklasson, G. A.; Edvinsson, T. Disentangling the intricate atomic short-range order and electronic properties in amorphous transition metal oxides. *Sci. Rep.* **2017**, *7*, 2044.
- (14) Smith, R. D. L.; Pasquini, C.; Loos, S.; Chernev, P.; Klingan, K.; Kubella, P.; Mohammadi, M. R.; González-Flores, D.; Dau, H. Geometric distortions in nickel (oxy)hydroxide electrocatalysts by redox inactive iron ions. *Energy Environ. Sci.* **2018**, *11*, 2476–2485.

- (15) Hall, D. S.; Lockwood, D. J.; Bock, C.; MacDougall, B. R. Nickel hydroxides and related materials: a review of their structures, synthesis and properties. *Proc. Royal Soc. A* **2015**, *471*, 20140792.
- (16) Kurzman, J. A.; Dettelbach, K. E.; Martinolich, A. J.; Berlinguette, C. P.; Neilson, J. R. Structural Characteristics and Eutaxy in the Photo-Deposited Amorphous Iron Oxide Oxygen Evolution Catalyst. *Chem. Mater.* **2015**, *27*, 3462–3470.
- (17) Trudel, S.; Crozier, E. D.; Gordon, R. A.; Budnik, P. S.; Hill, R. H. X-ray absorption fine structure study of amorphous metal oxide thin films prepared by photochemical metalorganic deposition. *J. Solid State Chem.* **2011**, *184*, 1025 – 1035.
- (18) Smith, R. D. L.; Prévot, M. S.; Fagan, R. D.; Trudel, S.; Berlinguette, C. P. Water Oxidation Catalysis: Electrocatalytic Response to Metal Stoichiometry in Amorphous Metal Oxide Films Containing Iron, Cobalt, and Nickel. *J. Am. Chem. Soc.* **2013**, *135*, 11580–11586.
- (19) Trudel, S.; Li, G.; Zhang, X.; Hill, R. H. Positive and Negative Lithography by Photochemical Metalorganic Deposition from Metal 2-ethylhexanoates. *J. Photopolym. Sci. Tec.* **2006**, *19*, 467–475.
- (20) Maniammal, K.; Madhu, G.; Biju, V. X-ray diffraction line profile analysis of nanostructured nickel oxide: Shape factor and convolution of crystallite size and microstrain contributions. *Physica E Low Dimens. Syst. Nanostruct.* **2017**, *85*, 214 – 222.
- (21) Seetawan, U.; Jugsujinda, S.; Seetawan, T.; Euvananont, C.; Junin, C.; Thanachayanont, C.; Chainaronk, P.; Amornkitbamrung, V. Effect of annealing temperature on the crystallography, particle size and thermopower of bulk ZnO. *Solid State Sci.* **2011**, *13*, 1599 – 1603.
- (22) Caruntu, G.; Rarig Jr, R.; Dumitru, I.; O'Connor, C. J. Annealing effects on the crystallite size and dielectric properties of ultrafine  $Ba_{1-x}Sr_xTiO_3$  ( $0 < x < 1$ ) powders synthesized through an oxalate-complex precursor. *J. Mater. Chem.* **2006**, *16*, 752–758.

- (23) Kamal, H.; Elmaghraby, E.; Ali, S.; Abdel-Hady, K. Characterization of nickel oxide films deposited at different substrate temperatures using spray pyrolysis. *J. Cryst. Growth* **2004**, *262*, 424 – 434.
- (24) Smith, R. D. L.; Pasquini, C.; Loos, S.; Chernev, P.; Klingan, K.; Kubella, P.; Mohammadi, M. R.; Gonzalez-Flores, D.; Dau, H. Spectroscopic identification of active sites for the oxygen evolution reaction on iron-cobalt oxides. *Nat. Comm.* **2017**, *8*, 2022.
- (25) Friebel, D.; Louie, M. W.; Bajdich, M.; Sanwald, K. E.; Cai, Y.; Wise, A. M.; Cheng, M.-J.; Sokaras, D.; Weng, T.-C.; Alonso-Mori, R.; Davis, R. C.; Bargar, J. R.; Nørskov, J. K.; Nilsson, A.; Bell, A. T. Identification of Highly Active Fe Sites in (Ni,Fe)OOH for Electrocatalytic Water Splitting. *J. Am. Chem. Soc.* **2015**, *137*, 1305–1313.
- (26) Pandya, K. I.; O’Grady, W. E.; Corrigan, D. A.; McBreen, J.; Hoffman, R. W. Extended x-ray absorption fine structure investigations of nickel hydroxides. *J. Phys. Chem.* **1990**, *94*, 21–26.
- (27) Görlin, M.; Chernev, P.; Ferreira de Araújo, J.; Reier, T.; Dresp, S.; Paul, B.; Krähnert, R.; Dau, H.; Strasser, P. Oxygen Evolution Reaction Dynamics, Faradaic Charge Efficiency, and the Active Metal Redox States of Ni–Fe Oxide Water Splitting Electrocatalysts. *J. Am. Chem. Soc.* **2016**, *138*, 5603–5614.
- (28) Nadesan, J. C. B. Oxygen Evolution on Nickel Oxide Electrodes. *J. Electrochem. Soc.* **1985**, *132*, 2957.
- (29) Stern, L.-A.; Hu, X. Enhanced oxygen evolution activity by NiOx and Ni(OH)<sub>2</sub> nanoparticles. *Faraday Discuss.* **2014**, *176*, 363–379.
- (30) Klaus, S.; Cai, Y.; Louie, M. W.; Trotochaud, L.; Bell, A. T. Effects of Fe Electrolyte Impurities on Ni(OH)<sub>2</sub>/NiOOH Structure and Oxygen Evolution Activity. *J. Phys. Chem. C* **2015**, *119*, 7243–7254.

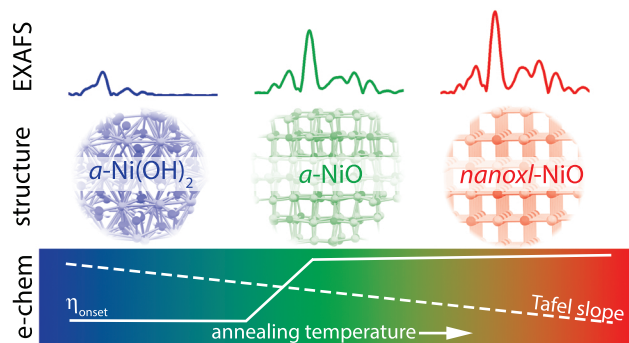
- (31) McCrory, C. C. L.; Jung, S.; Ferrer, I. M.; Chatman, S. M.; Peters, J. C.; Jaramillo, T. F. Benchmarking Hydrogen Evolving Reaction and Oxygen Evolving Reaction Electrocatalysts for Solar Water Splitting Devices. *J. Am. Chem. Soc.* **2015**, *137*, 4347–4357.
- (32) Srinivasan, V.; Weidner, J. W. Studies on the Capacitance of Nickel Oxide Films: Effect of Heating Temperature and Electrolyte Concentration. *J. Electrochem. Soc.* **2000**, *147*, 880.
- (33) Smith, R. D. L.; Berlinguette, C. P. Accounting for the Dynamic Oxidative Behavior of Nickel Anodes. *J. Am. Chem. Soc.* **2016**, *138*, 1561–1567.
- (34) Carpenter, M. K.; Conell, R. S.; Corrigan, D. A. The electrochromic properties of hydrous nickel oxide. *Sol. Energy Mater.* **1987**, *16*, 333 – 346.
- (35) Kadam, L.; Patil, P. Studies on electrochromic properties of nickel oxide thin films prepared by spray pyrolysis technique. *Sol. Energy Mater Sol.* **2001**, *69*, 361 – 369.
- (36) Liu, Q.; Chen, Q.; Zhang, Q.; Xiao, Y.; Zhong, X.; Dong, G.; Delplancke-Ogletree, M.-P.; Terryn, H.; Baert, K.; Reniers, F.; Diao, X. In situ electrochromic efficiency of a nickel oxide thin film: origin of electrochemical process and electrochromic degradation. *J. Mater. Chem. C* **2018**, *6*, 646–653.
- (37) Damjanovic, A.; Dey, A.; Bockris, J. Kinetics of oxygen evolution and dissolution on platinum electrodes. *Electrochim. Acta* **1966**, *11*, 791 – 814.
- (38) Rossmesl, J.; Qu, Z.-W.; Zhu, H.; Kroes, G.-J.; Nørskov, J. Electrolysis of water on oxide surfaces. *J. Electroanal. Chem.* **2007**, *607*, 83 – 89.
- (39) Li, Y.-F.; Liu, Z.-P.; Liu, L.; Gao, W. Mechanism and Activity of Photocatalytic Oxygen Evolution on Titania Anatase in Aqueous Surroundings. *J. Am. Chem. Soc.* **2010**, *132*, 13008–13015.
- (40) Morishita, T. High Density Amorphous Form and Polyamorphic Transformations of Silicon. *Phys. Rev. Lett.* **2004**, *93*, 055503.

- (41) Sheng, H. W.; Liu, H. Z.; Cheng, Y. Q.; Wen, J.; Lee, P. L.; Luo, W. K.; Shastri, S. D.; Ma, E. Polyamorphism in a metallic glass. *Nat. Mater.* **2007**, *6*, 192–197.
- (42) Rooksby, H. P. Structure of Nickel Oxide. *Nature* **1943**, *152*, 304–304.
- (43) Taşköprü, T.; Zor, M.; Turan, E. Structural characterization of nickel oxide/hydroxide nanosheets produced by CBD technique. *Mater. Res. Bull.* **2015**, *70*, 633 – 639.
- (44) Wu, M.-S.; Hsieh, H.-H. Nickel oxide/hydroxide nanoplatelets synthesized by chemical precipitation for electrochemical capacitors. *Electrochim. Acta* **2008**, *53*, 3427 – 3435.
- (45) Bediako, D. K.; Lassalle-Kaiser, B.; Surendranath, Y.; Yano, J.; Yachandra, V. K.; Nocera, D. G. Structure–Activity Correlations in a Nickel–Borate Oxygen Evolution Catalyst. *J. Am. Chem. Soc.* **2012**, *134*, 6801–6809.
- (46) Li, L.-F.; Li, Y.-F.; Liu, Z.-P. Oxygen Evolution Activity on NiOOH Catalysts: Four-Coordinated Ni Cation as the Active Site and the Hydroperoxide Mechanism. *ACS Catal.* **2020**, *10*, 2581–2590.
- (47) Tripkovic, V.; Vegge, T. Potential- and Rate-Determining Step for Oxygen Reduction on Pt(111). *J. Phys. Chem. C* **2017**, *121*, 26785–26793.
- (48) Kuai, C.; Zhang, Y.; Han, L.; Xin, H. L.; Sun, C.-J.; Nordlund, D.; Qiao, S.; Du, X.-W.; Lin, F. Creating compressive stress at the NiOOH/NiO interface for water oxidation. *J. Mater. Chem. A* **2020**, *8*, 10747–10754.
- (49) Shuttleworth, I. G. Binding Site Transitions Across Strained Oxygenated and Hydroxylated Pt(111). *Open Chem.* **2018**, *7*, 356–369.
- (50) Liu, F.; Wu, C.; Yang, G.; Yang, S. CO Oxidation over Strained Pt(100) Surface: A DFT Study. *J. Phys. Chem. C* **2015**, *119*, 15500–15505.

- (51) Tao, H. B.; Zhang, J.; Chen, J.; Zhang, L.; Xu, Y.; Chen, J. G.; Liu, B. Revealing Energetics of Surface Oxygen Redox from Kinetic Fingerprint in Oxygen Electrocatalysis. *J. Am. Chem. Soc.* **2019**, *141*, 13803–13811.
- (52) Shinagawa, T.; Garcia-Esparza, A. T.; Takanabe, K. Insight on Tafel slopes from a microkinetic analysis of aqueous electrocatalysis for energy conversion. *Sci. Rep.* **2015**, *5*, 13801.
- (53) Surendranath, Y.; Bediako, D. K.; Nocera, D. G. Interplay of oxygen-evolution kinetics and photovoltaic power curves on the construction of artificial leaves. *Proc. Natl. Acad. Sci. U.S.A.* **2012**, *109*, 15617–15621.
- (54) Trotochaud, L.; Young, S. L.; Ranney, J. K.; Boettcher, S. W. Nickel–Iron Oxyhydroxide Oxygen-Evolution Electrocatalysts: The Role of Intentional and Incidental Iron Incorporation. *J. Am. Chem. Soc.* **2014**, *136*, 6744–6753.
- (55) Patterson, A. L. The Scherrer Formula for X-Ray Particle Size Determination. *Phys. Rev.* **1939**, *56*, 978–982.
- (56) Langford, J. I.; Wilson, A. J. C. Scherrer after sixty years: A survey and some new results in the determination of crystallite size. *J. Appl. Crystallogr.* **1978**, *11*, 102–113.
- (57) Tauc, J. Optical properties and electronic structure of amorphous Ge and Si. *Mater. Res. Bull.* **1968**, *3*, 37 – 46.
- (58) Ravel, B.; Newville, M. ATHENA, ARTEMIS, HEPHAESTUS: data analysis for X-ray absorption spectroscopy using IFEFFIT. *J. Synchrotron Radiat.* **2005**, *12*, 537–541.
- (59) Kraft, S.; Stümpel, J.; Becker, P.; Kuetgens, U. High resolution x-ray absorption spectroscopy with absolute energy calibration for the determination of absorption edge energies. *Rev. Sci. Instrum.* **1996**, *67*, 681–687.
- (60) Mustre de Leon, J.; Rehr, J. J.; Zabinsky, S. I.; Albers, R. C. Ab initio curved-wave x-ray-absorption fine structure. *Phys. Rev. B* **1991**, *44*, 4146–4156.

- (61) Rehr, J. J.; Albers, R. C. Scattering-matrix formulation of curved-wave multiple-scattering theory: Application to x-ray-absorption fine structure. *Phys. Rev. B* **1990**, *41*, 8139–8149.
- (62) Biesinger, M. C.; Payne, B. P.; Lau, L. W. M.; Gerson, A.; Smart, R. S. C. X-ray photoelectron spectroscopic chemical state quantification of mixed nickel metal, oxide and hydroxide systems. *Surf. Interface Anal.* **2009**, *41*, 324–332.
- (63) Noam, E.; Eliezer, G. Physical Electrochemistry: Fundamentals, Techniques, and Applications. *Wiley-VCH, Weinheim* **2018**,
- (64) Manjunatha, K. N.; Paul, S. Investigation of optical properties of nickel oxide thin films deposited on different substrates. *Appl. Surf. Sci.* **2015**, *352*, 10 – 15.
- (65) Nalage, S.; Chougule, M.; Sen, S.; Joshi, P.; Patil, V. Sol–gel synthesis of nickel oxide thin films and their characterization. *Thin Solid Films* **2012**, *520*, 4835 – 4840.
- (66) Itapu, S.; Borra, V.; Mossayebi, F. A Computational Study on the Variation of Bandgap Due to Native Defects in Non-Stoichiometric NiO and Pd, Pt Doping in Stoichiometric NiO. *J. Phys. Condens. Matter* **2018**, *3*.

# Table of content graphic



**Supplementary Information.**

**Structural evolution in photodeposited  
nickel(oxy)hydroxide oxygen evolution  
electrocatalysts**

Martin A. W. Schoen,<sup>a</sup> Nicholas M. Randell,<sup>a</sup> Oliver Calderon,<sup>a</sup> Santiago Jimenez Villegas,<sup>a</sup> Zachary Thomson,<sup>a</sup> Roman Chernikov,<sup>b</sup> and Simon Trudel<sup>\* a\*</sup>

<sup>a</sup> *Department of Chemistry and Institute for Quantum Science and Technology, University of Calgary, 2500 University Dr NW, Calgary, AB, T2N 1N4, Canada.*

<sup>b</sup> *BIOXAS Beamline, Canadian Light Source, 44 Innovation Boulevard, Saskatoon, SK, S7N 2V3, Canada.*

\* E-mail: [trudels@ucalgary.ca](mailto:trudels@ucalgary.ca)

## Experimental Section

**Chemicals and substrates** Ni(II) 2-ethylhexanoate (**Ni(2-ethex)**<sub>2</sub>, 78 % in mineral spirits) was purchased from STREM Chemicals, methyl-isobutyl-ketone (MIBK) was purchased from Alpha Aesar, potassium hydroxide obtained from EMD Millipore. All were used as-received without further purification. 99 % NiO powder for XRD and EXAFS standards was purchased from Alpha Aesar. Fluorine-doped tin oxide (7 Ω / sq.) on glass substrates (FTO) were acquired from Hartford Glass Company. FTO substrates were cleaned by 5 minute sonication in acetone, which was not allowed to dry and rinsed off with isopropanol and subsequently dried in N<sub>2</sub>. SiO<sub>2</sub> (50 nm) / Si substrates were prepared by cleaning in-house cut Si(100) wafers (University Wafers, B-doped, 500 μm thick), using the same cleaning procedure as for the FTO substrates. A thermal oxide layer of approximately 50 nm thickness (verified by ellipsometry) was produced by annealing substrates in air for 5 h at 1000 °C in a furnace.

Fe-free KOH was prepared following previously reported methods.<sup>54</sup>

**Thin film deposition** Amorphous NiO<sub>x</sub> films were deposited by ultraviolet-initiated photochemical deposition, as previously reported.<sup>8,18,19</sup> Briefly, **Ni(2-ethex)**<sub>2</sub> was diluted to 15 wt% in MIBK and the resulting precursor solution spin coated (Laurel, 3000 rpm, 60 s) on clean FTO substrates, or SiO<sub>2</sub>(50 nm)/ Si substrates. These films were then irradiated with a UV light (Atlantic UV lamp model GPH893T5VH/HO/4PSE High Ozone, λ = 185 nm and 254 nm) for 24 h, ensuring a complete decomposition of the ligands, producing a homogeneous thin film of NiO<sub>x</sub>. The films were used as-prepared (no anneal), or annealed in air at temperatures ranging between 100 and 600 °C for samples on FTO substrates, and up to 1000 °C for samples on Si substrates. Samples are labeled as **Ni-AP** for the as-prepared samples and as **Ni-100**, **Ni-200**, **Ni-300**, etc. for the annealed samples.

**X-ray diffraction (XRD)** XRD was performed with a Bruker D8 Advance Eco with a Cu K<sub>α</sub> tube (λ = 1.5406) in the vicinity of the (111) and (200) peaks for NiO (2θ = 36 – 46 °, step width 0.04 °, and 3 s averaging per step). The crystallite size *d*<sub>cr</sub> was estimated using the Scherrer equation<sup>55</sup>

$$d_{\text{cr}} = \frac{K\lambda}{\beta \cos\theta}, \quad (\text{S1})$$

where  $K$  is the shape factor (a value of 0.9 was used),  $\lambda$  is the x-ray wavelength,  $\beta$  is the instrument-broadening corrected full width at half maximum (FWHM) of the XRD peak, and  $\theta$  is the Bragg angle. The XRD peak is fit with a Lorentzian function to extract the peak's FWHM. The FWHM is corrected for instrument broadening, which is determined as the FWHM of a bulk powdered NiO sample ( $\beta = \beta_{\text{measured}} - \beta_{\text{NiO}}$ ). Error bars are estimated from the  $2\sigma$  confidence interval of the Lorentzian fits with an additional 10 % error from the uncertainty in shape factor  $K$  which typically ranges from 0.8 to 1 for similar samples.<sup>56</sup>

**Ultraviolet-visible (UV-vis) spectroscopy** UV-vis spectroscopy was performed with a Cary 5000 spectrometer equipped with a DRA-2500 diffuse reflectance attachment between 0.6 eV and 5 eV. Band gaps were determined following a Tauc analysis.<sup>57</sup> Errors are estimated from  $2\sigma$  confidence intervals of the linear fit to the Tauc plot.

**X-ray absorption spectroscopy (XAS)** X-ray absorption spectra at the Ni K-edge were collected at the BioXAS beamline (Main Endstation) of the Canadian Light Source. A Si(220) double crystal monochromator was used. X-ray fluorescence spectra were recorded with a 32-channel energy-discriminating Canberra Ge fluorescence detector. Spectra were acquired from 150 eV below the absorption edge to  $k = 14 \text{ \AA}^{-1}$ . Two series of samples were measured: first, annealed NiO<sub>x</sub> films; second, a series of corresponding electrochemically pre-treated films. For the latter series the samples were put in the electrochemical cell described below and held at a potential of 1.9 V vs. RHE ( $\approx 15 \text{ mA cm}^{-2}$ ) for 120 s, rinsed, dried off, and measured *ex situ*. These *post operando* (PO) measured samples are labeled as **Ni-AP-PO**, **Ni-100-PO**, **Ni-200-PO**, etc. Samples were measured within 3 h of electrochemical treatment, since visible discoloration of the treated samples occurred after 8 h in ambient conditions. Additionally, spectra of powdered NiO and Ni(OH)<sub>2</sub> were recorded as comparative reference spectra. All spectra were analyzed using the Demeter software package version 0.9.26,<sup>58</sup> after normalization and flattening. The energy was calibrated using the absolute energy list by Kraft,<sup>59</sup> using a Ni foil. The following data

processing settings were used: pre-edge range -150 eV to -50 eV, normalization range 200 eV to 700 eV,  $R_{\text{bkg}} = 1.1 \text{ \AA}$ , spline range  $k = 0-14 \text{ \AA}^{-1}$ , and Fourier transform in  $k$  from 3 to  $12 \text{ \AA}^{-1}$ . Scattering paths were calculated using FEFF6<sup>60,61</sup> based on a structural model of NiO. Fits are weighted by  $k$  and  $k^3$ . Error bars for the extracted parameters are the standard errors calculated by Artemis.

**X-ray photoelectron spectroscopy (XPS)** X-ray photoelectron spectroscopy (XPS) was performed using a Kratos Analytical XPS spectrometer (nanoFAB Fabrication and Characterization Centre, University of Alberta) with a monochromatic Al  $K_{\alpha}$  source ( $\lambda = 1486.6 \text{ eV}$ ) and a  $2 \text{ mm}^2$  probing area. All spectra were analyzed using CasaXPS software (<http://www.casaxps.com/>). Spectra were corrected by calibrating all peaks to the adventitious C 1s peak signal at 284.5 eV. A Shirley-type background was used, and curve fitting was performed using a combination of Gaussian and Lorentzian [GL(85)] profiles. Fitting of the high-resolution Ni spectra was only performed on the Ni 2p  $_{3/2}$  peak following the method outlined in Ref. 62. NiO, Ni(OH)<sub>2</sub>, and NiOOH peaks with constraint fit parameters<sup>62</sup> are used to model the data.

**Electrochemistry** Electrochemical measurements were carried out using a CH Instruments 660D potentiostat. A Pt mesh was used as a counter electrode and a saturated Ag/AgCl electrode used as a reference electrode, sitting in a Luggin capillary. The supporting solution is 1 M KOH aqueous solution. Fe-free KOH was used to avoid electrolyte impurities in the films.<sup>30,54</sup> Calibration of the Ag/AgCl (sat. KCl) electrode against a 1 mM aqueous solution of Na<sub>4</sub>[Fe(CN)<sub>6</sub>] ( $E = 0.361 \text{ V vs NHE}$ ) was regularly performed throughout the study thus obtaining potential vs NHE. The overpotential  $\eta$  can then be calculated<sup>18</sup> as  $\eta = E_{\text{applied vs NHE}} + 0.059 \cdot \text{pH} + 1.23$ . All measurements are reported as current densities, normalized by the geometric surface area. Unless specified otherwise, all potentials are against the reversible hydrogen electrode (RHE).

Cyclic voltammetry (CV) was carried out at two different sweep rates of 0.1 and 0.01 V s<sup>-1</sup>. CVs were run until the catalyst was stable.  $\eta$  at catalytic onset and at a current density of 10 mA/cm<sup>2</sup> were then determined. Catalytic onset was defined as the start of the Tafel region. Step-wise voltammetry was carried out in the linear Tafel region. At each step the catalyst was

given 40 s to stabilize before measuring. The Tafel slope was then extracted from the linear section of the  $\log(j)$  vs.  $\eta$  plot. All electrochemical measurements were measured in triplicate and reported values are the average of these measurements. Errors are estimated from the standard deviation of the triplicate results.

The double layer capacitance  $C_{dl}$  was determined by first running CVs from 0.9 to 2.4 V vs RHE until a steady state is reached and then measuring CVs in the non-faradaic region before any catalytic activity at scan rates  $\nu$  ranging from 0.005 to 0.1 V s<sup>-1</sup>.  $C_{dl}$  is then calculated from the slope of  $j$  at 0.075 V vs  $\nu$ , via  $j = C_{dl}\nu$ .<sup>63</sup> Error bars are calculated from the  $2\sigma$  confidence intervals of the linear fit.

**Electrochromism** Samples were measured *in-situ* submerged in a 1 M KOH solution in a quartz cuvette, with the Pt mesh counter electrode and Ag/AgCl(sat'd) reference electrode submerged in the cuvette and an adjacent Luggin capillary, respectively. Spectra in the visible range (350 nm to 800 nm) were taken in the following order: before applying a current, after running approx. 10 CVs (0.9 V to 2.4 V vs RHE at 0.1 and 0.01 V s<sup>-1</sup>), at the potential of the first oxidation peak, at 1.9 V vs RHE, at 2.4 V vs RHE, at open current potential, and after running a regeneration cycle. 100 % transmission for these measurements was defined as the transmission of the KOH-filled quartz cuvette. Regeneration cycles consisted of 3 CVs from 0.9 to 1.1 V vs RHE at 0.01 V s<sup>-1</sup>, recovering maximal transmission after applying the potential.

Kinetic measurements were taken by measuring transmission over time at 450 nm and applying a single voltage step to the potential of the first oxidation peak, 1.9 V vs RHE, or 2.4 V vs RHE and turning off the potential once a steady state is achieved. Similarly, transmission is measured during CVs from 0.9 to 2.4 V vs RHE at 0.1 V s<sup>-1</sup> and 0.01 V s<sup>-1</sup>.

# Figures

## Optical properties

Diffuse reflectance spectra and the Kubelka-Munk parameter for the direct band gap  $(F(R)h\nu)^2$  are plotted in Fig. S1a for **Ni-100**, **Ni-300**, and **Ni-600** on Si wafers. The spectra show a single decrease in reflectivity (increase in absorption  $\approx (F(R)h\nu)^2$ ) for each sample, consistent with a band gap corresponding to that energy. Each sample exhibits an additional absorption peak at approximately 1 eV, that is independent of  $T_{\text{anneal}}$  (data not shown), which we attribute to the Si substrate. The band gaps increase almost linearly with  $T_{\text{anneal}}$  from 3.8 eV for **Ni-AP** to  $>5.7$  eV for **Ni-600** (Fig. S1b). The range of our instrumentation is limited to 5 eV therefore, we can only give a lower limit for the band gaps above 5 eV. Our determined band gaps present a significant blue shift compared to literature values, where band gaps range from 3.2 eV to 4.5 eV<sup>64,65</sup> for nickel oxides depending on sample deposition technique and substrate. Additionally, computations have shown that relatively small changes in stoichiometry significantly influence the band gap.<sup>66</sup> However, we have not found precedence for the exceedingly large band gaps of our sample series. At this point the origin of this discrepancy is not known and warrants further investigation, which is beyond the scope of this present work.

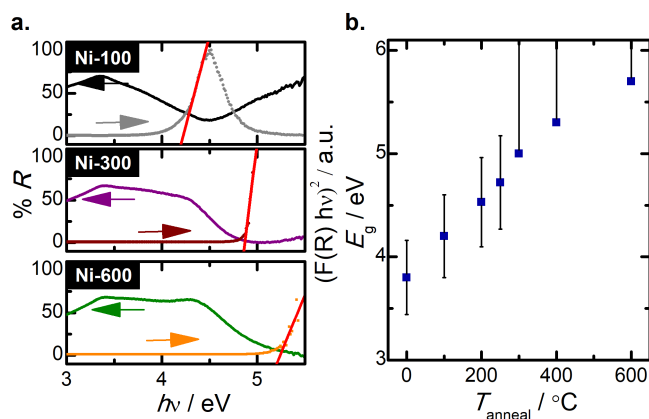


Figure S1: a. UV-Vis diffuse reflectance spectra for **Ni-100**, **Ni-300**, and **Ni-600**; Diffuse reflectance on lhs axis and  $(F(R)h\nu)^2$  on rhs axis. b. determined band gap plotted against annealing temperature.

## X-ray photoelectron spectroscopy

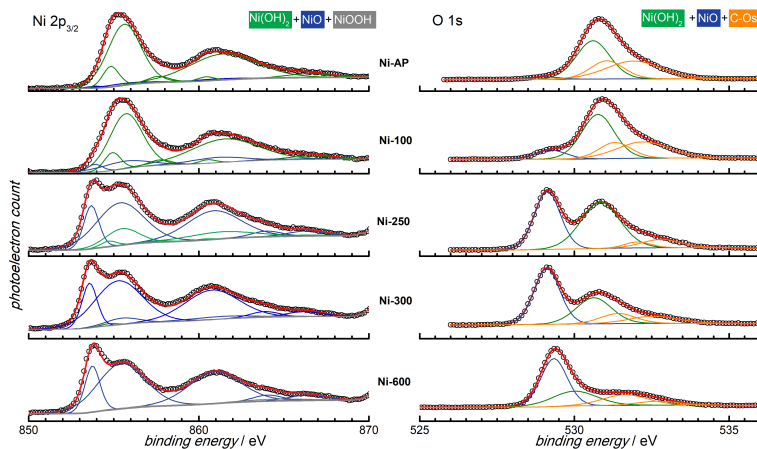


Figure S2: Ni p3/2 (lhs) and O 1s (rhs) XPS spectra of all samples. Fits to the spectra are plotted as red lines and individual fit components are plotted as lines in colors denoted.

## **X-ray absorption spectroscopy**

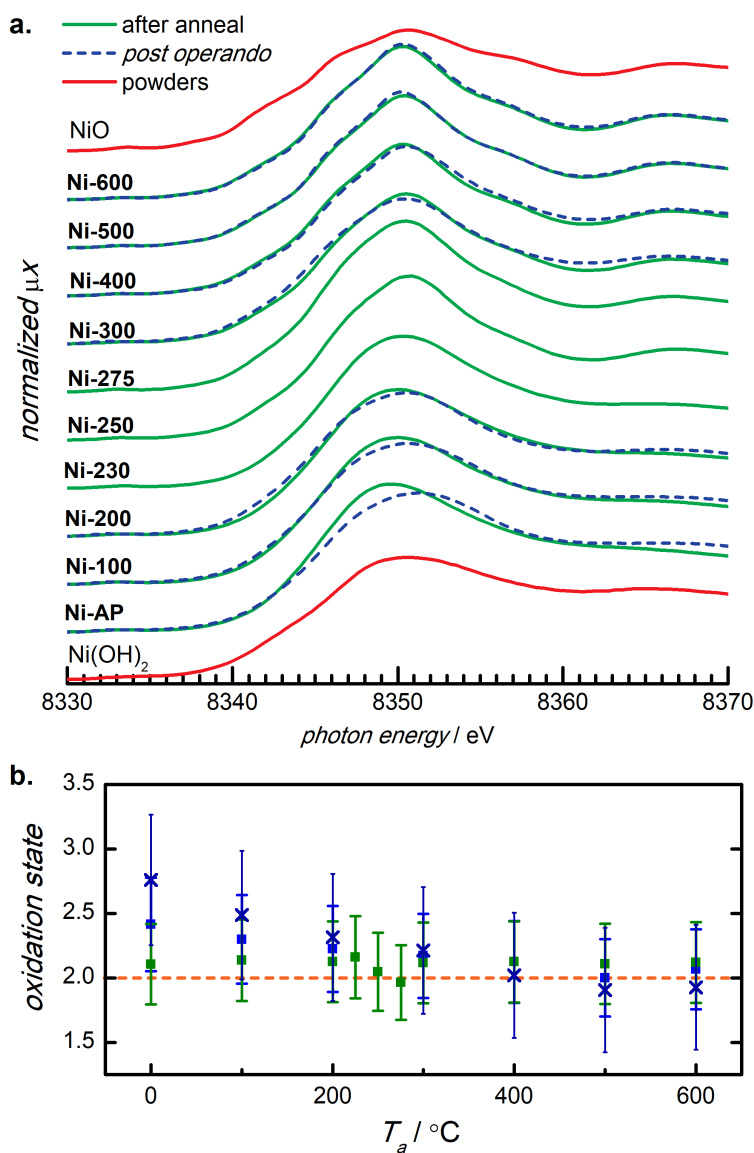


Figure S3: a. XANES spectra of samples **Ni-AP** through **Ni-600** are plotted in green and post-operando series is plotted in blue dashed lines. Reference spectra of Ni(OH)<sub>2</sub> and NiO are graphed in red. b. shows the oxidation state plotted against annealing temperature. Green and blue squares represent the oxidation states determined from XANES edge position for annealed and PO series, respectively. Blue crosses show the oxidation state of the PO series determined from oxygen bond distances.

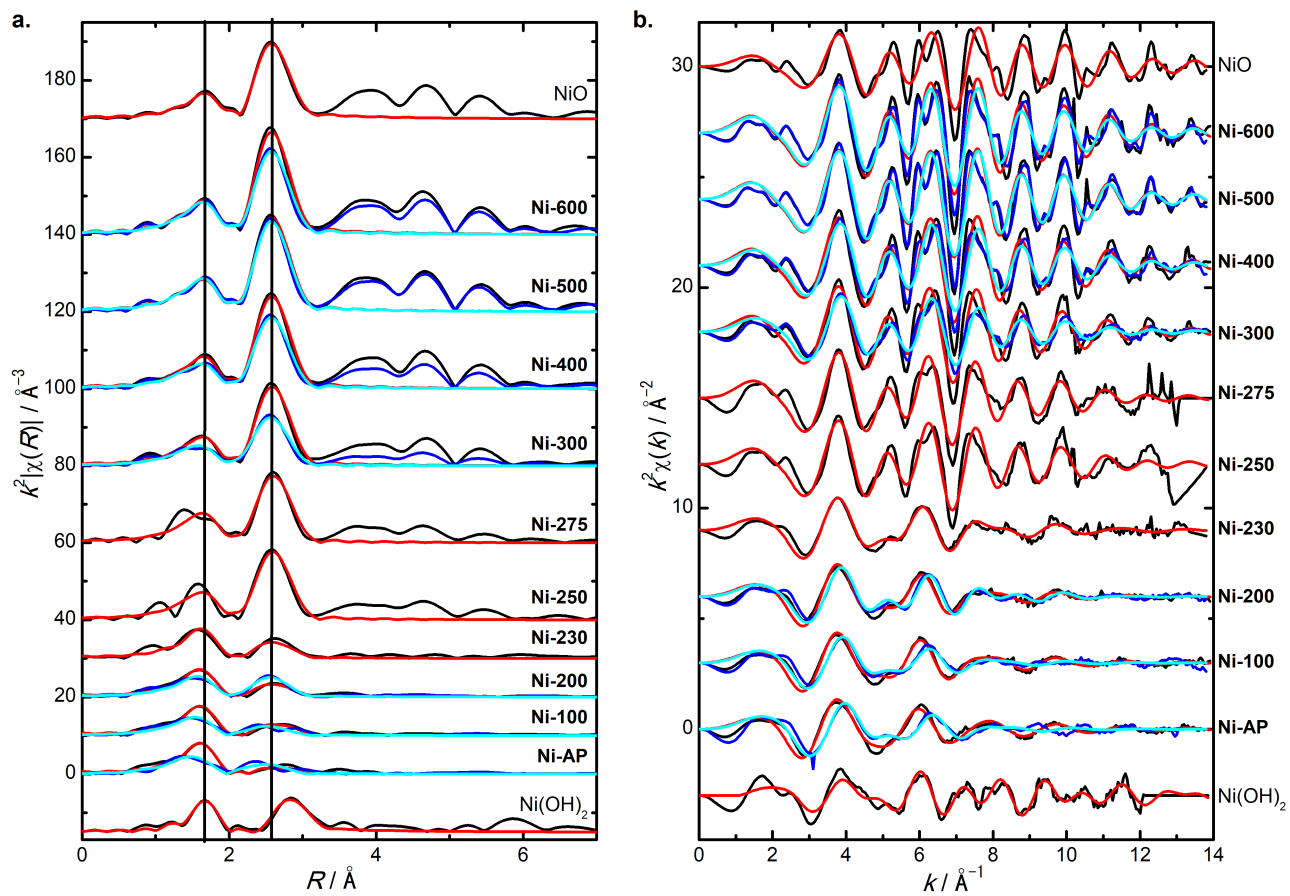


Figure S4: a. Fourier transform of the EXAFS signal and b. EXAFS signal for all samples. Data and fit for the annealed series are plotted in black and red, Data and fit for the PO series in dark blue and light blue.

## Electrochemistry

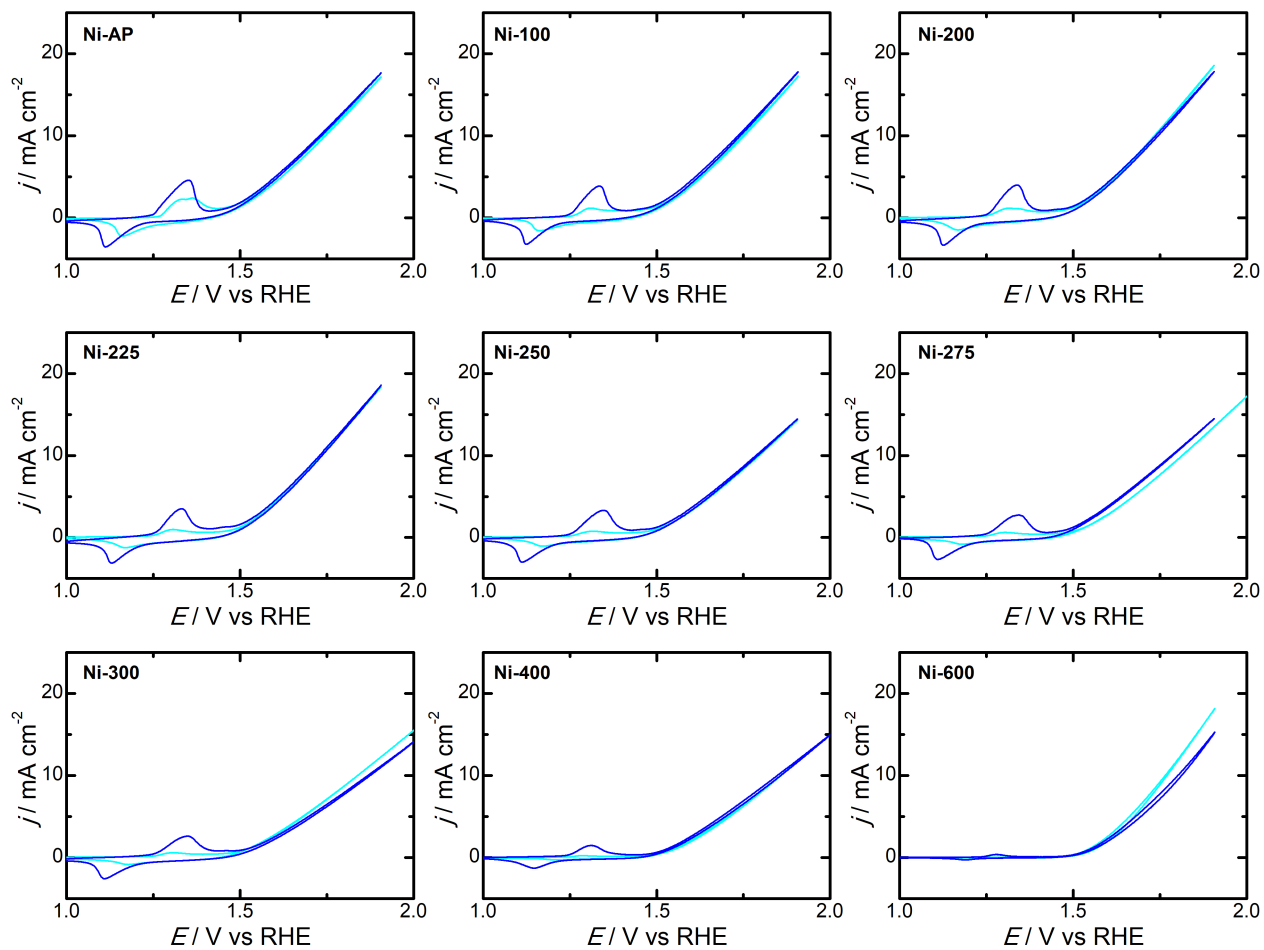


Figure S5: CVs of first run (light blue lines) and in steady state (dark blue lines). For each  $T_{\text{anneal}}$  one representative sample it picked for clarity.

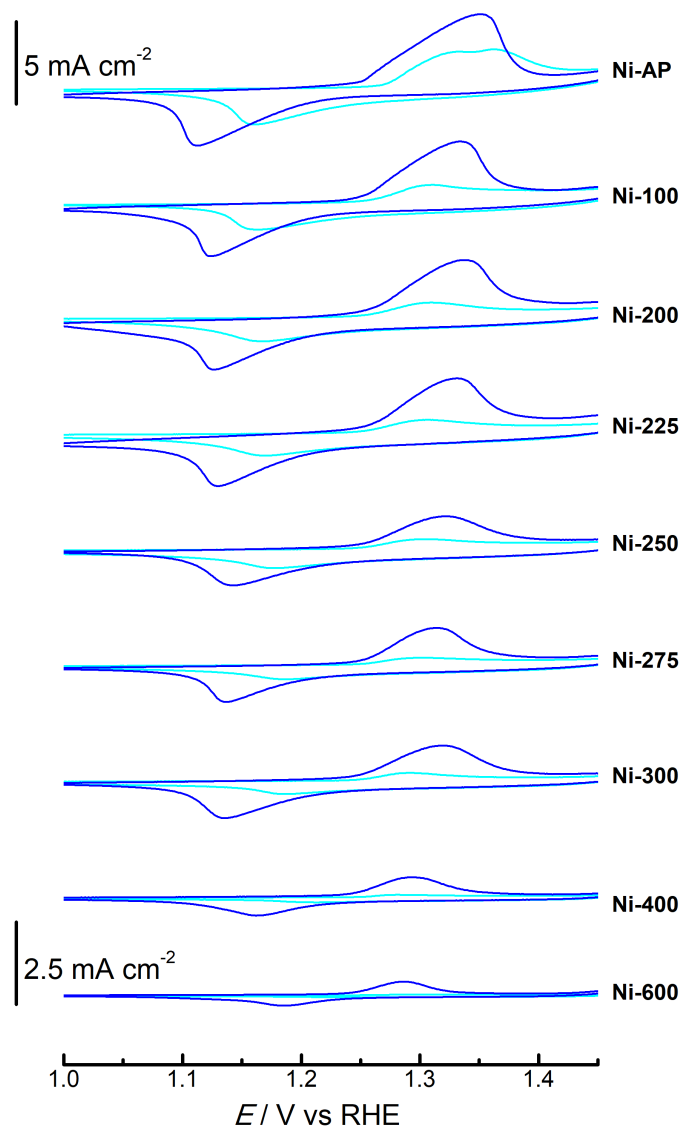


Figure S6: Emphasis on the Ni redox peaks of the pre-catalysis region of the CVs. Note the vertical scale for the **Ni-600** sample is amplified for clarity.

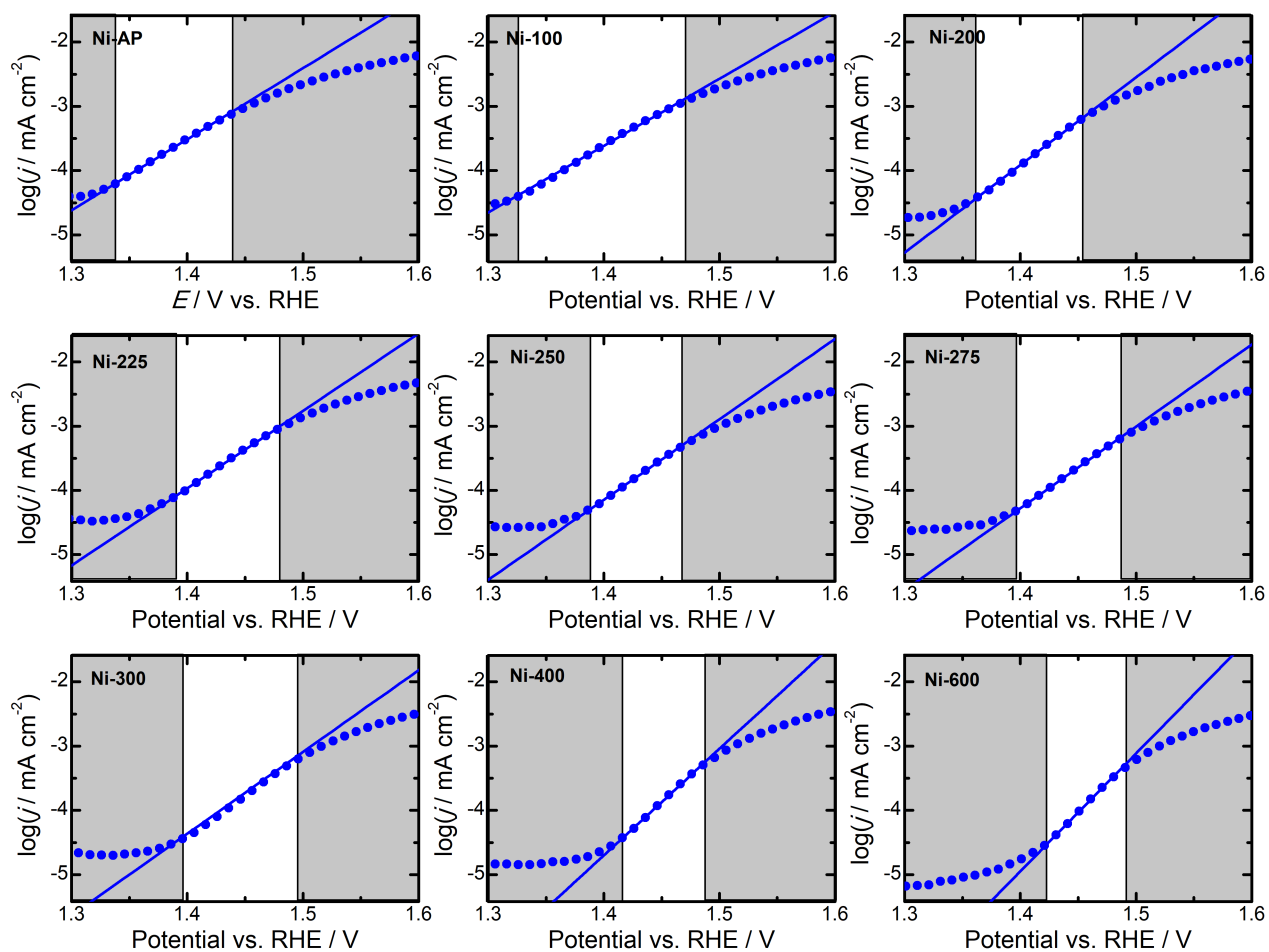


Figure S7: Representative steady-state current densities as a function of applied potential. Lines are linear fits used to determine the Tafel slope, data in the shaded regions excluded from fit.

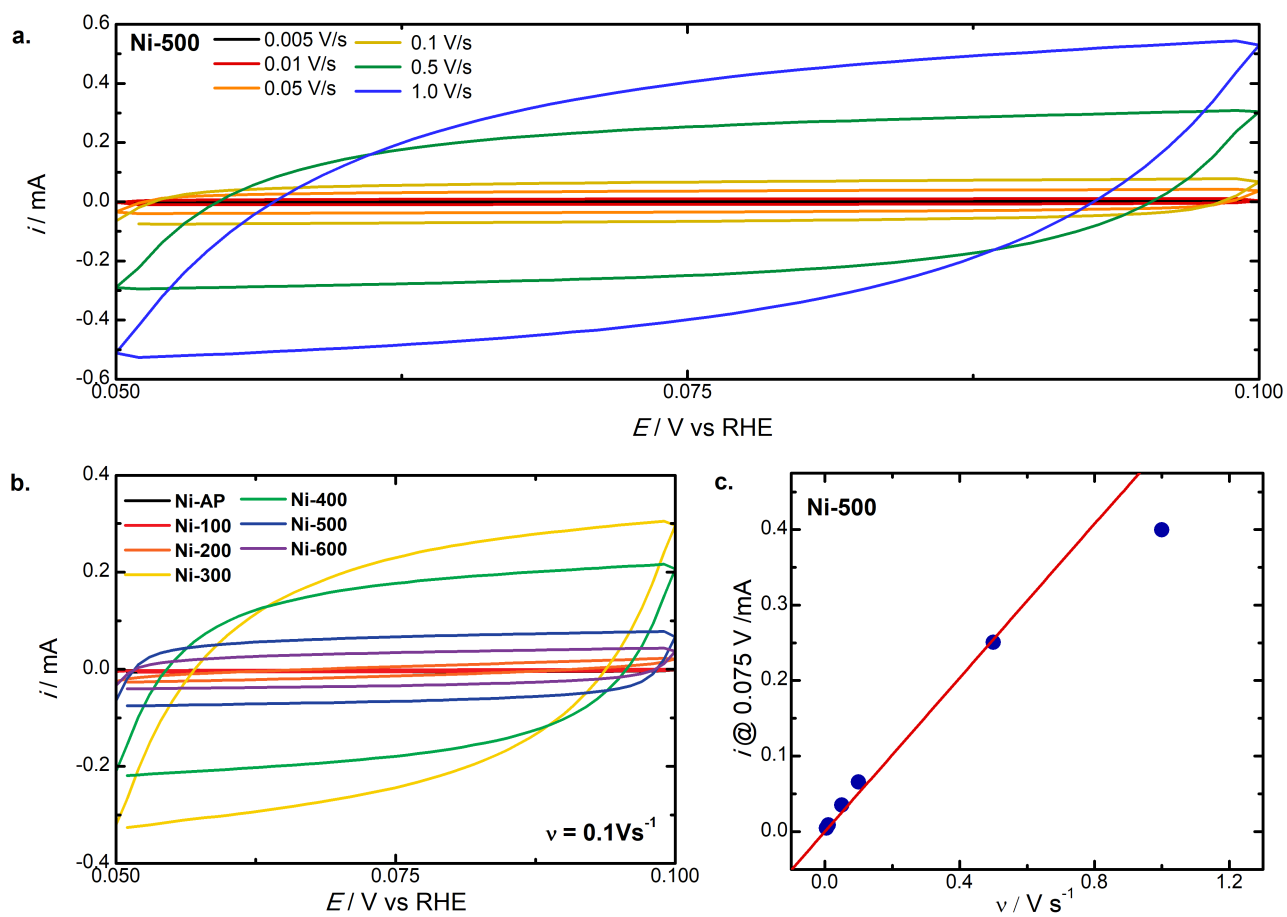


Figure S8: a. CVs of sample **Ni-500** at sweep rates from 0.005 V/s to 1 V/s. b. CVs for at a sweep rate of 0.01 V/s for samples **Ni-AP** through **Ni-600**. c. current density at 0.075 V/mA plotted against sweep rate. The red line is a linear fit to the linear range of the data to extract  $C_{dl}$ .

## Electrochromism

**Steady-state electrochromism.** The *in situ* UV-vis transmission spectra measured under conditions described in Fig. S10a are presented in Fig. S10b-d for samples **Ni-100**, **Ni-300**, and **Ni-600**. Initially, all samples are transparent and for **Ni-300** through **Ni-600** their *in situ* spectra without applied potential mimic the FTO spectrum closely, while spectra at lower  $T_{\text{anneal}}$  differ slightly from the FTO spectrum (Fig. S9). After a single CV measurement (step 2) is performed **Ni-100** persists in a lightly colored state, while the other two samples experience little to no coloration. With applied potential all samples color further. However, sample coloration decreases with  $T_{\text{anneal}}$  at the anodic oxidation peak  $E_{\text{p,a}}$  (step 3), 1.9 V vs RHE (step 4), and 2.4 V vs RHE (step 5). The noise in steps 4 and 5 is attributed to oxygen bubbles formed under OER conditions, which scatter light. While spectra for **Ni-100** change from convex to concave shape with applied potential, the spectra retain their convex shape for higher  $T_{\text{anneal}}$ . Furthermore, a marked increase in coloring is observed for all samples in step 5. Back at open current potential (OCP, step 6) the coloration reverts back to states similar to step 3. The discolored state is fully regained for all samples with regeneration (step 7, see Methods section). This regeneration is fully reproducible from any state of coloration.

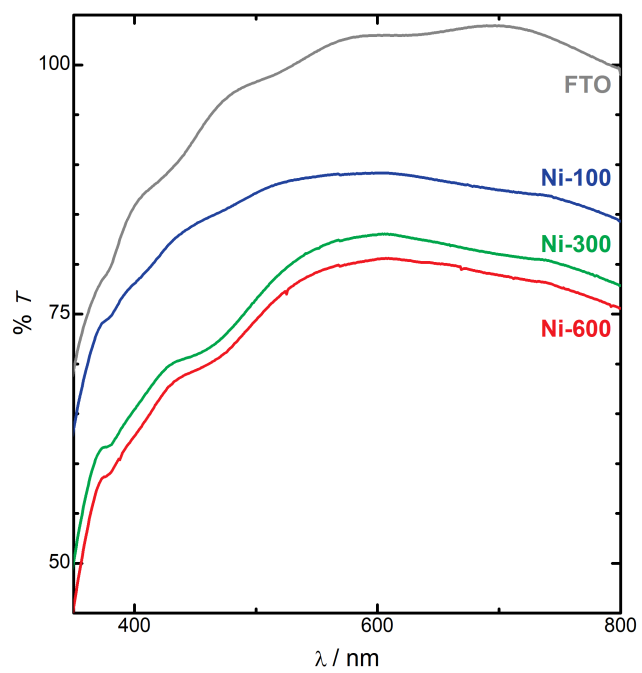


Figure S9: *In situ* spectra of **Ni-100**, **Ni-300**, and **Ni-600** compared to blank FTO substrate.

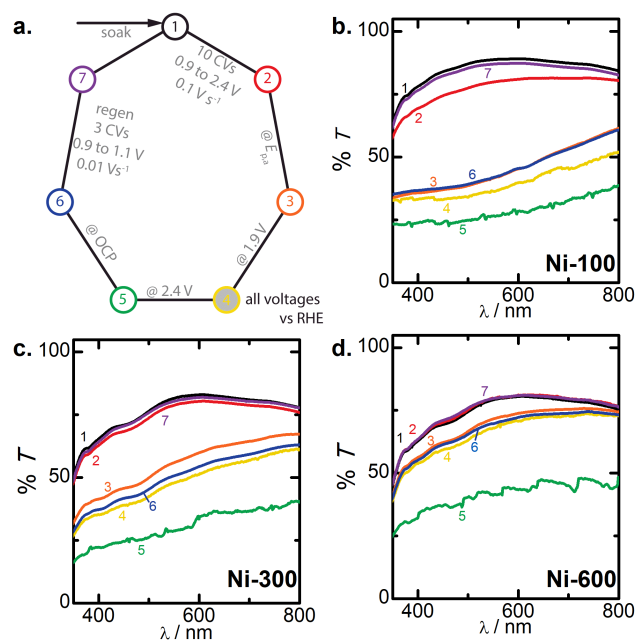


Figure S10: UV-Vis transmission spectra of samples annealed at b. 100 °C, c. 300 °C, and d. 600 °C from  $\lambda = 400$  nm to 800 nm taken in-situ in the electrochromic cell. 100 % transmission is for the KOH filled cell at 800 nm. Numbers signify the following steps in order: 1 immersed in KOH, 2 after one CV, 3 at pre-oxidation peak potential, 4 at 1.9 V (vs RHE), 5 at 2.4 V (vs RHE), 6 at open current potential, 7 after regeneration cycle. a. shows a schematic of this measurement cycle.

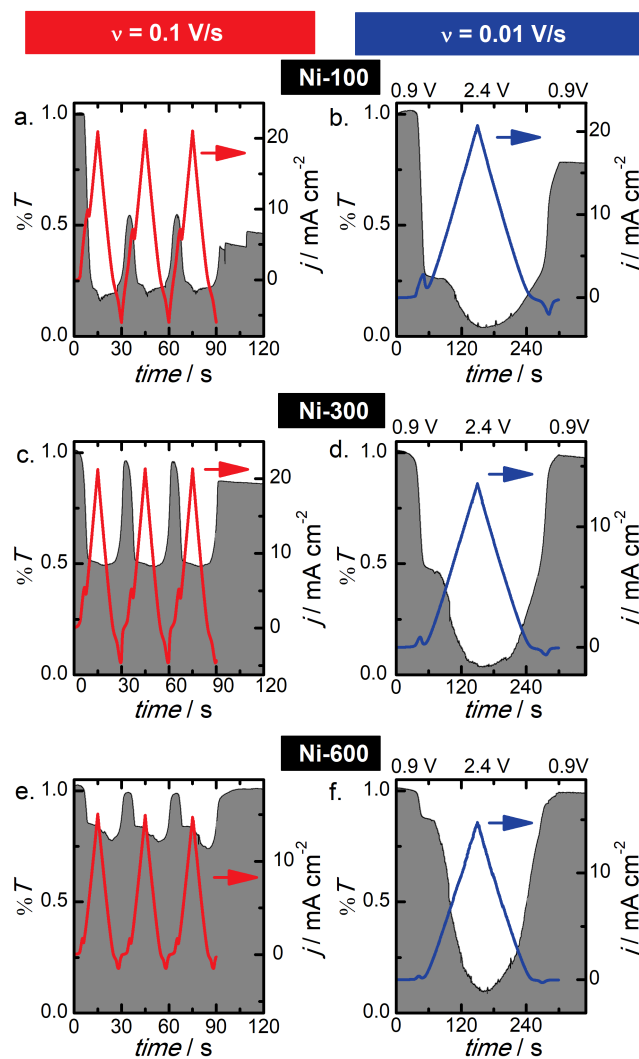


Figure S11: Transmission at  $\lambda = 450$  nm plotted against time (black lines, lhs and bottom axis) and current density plotted against applied potential (gray lines, rhs and top axis) for samples annealed at a. and b. 100 °C, c. and d. 300 °C, and e. and f. 600 °C. a., c., and e. show three CVs at 0.1 V/s sweep rate and b., d., and f. show single CVs at 0.01 V/s.

## Tables

Table S1: Constrained XPS fit parameters for each component. P1 and A1 refer to peak 1 position and area, respectively.

Constrained parameters	NiO	Ni(OH) <sub>2</sub>	NiOOH
Peak 2 position (eV)	P1 + 1.7	P1+0.8	P1 + 0.7
Peak 2 area	A1 × 3.091	A1 × 6.12	A1 × 0.9
Peak 3 position (eV)	P1 + 7.2	P1 + 2.8	P1 + 1.06
Peak 3 area	A1 × 2.378	A1 × 0.405	A1 × 0.703
Peak 4 position (eV)	P1 + 10.3	P1 + 5.6	P1 + 1.84
Peak 4 area	A1 × 0.252	A1 × 0.189	A1 × 1.5
Peak 5 position (eV)	P1 + 12.6	P1 + 6.6	P1 + 3.17
Peak 5 area	A1 × 0.273	A1 × 5.297	A1 × 0.63
Peak 6 position (eV)		P1 + 11.6	P1 + 6.37
Peak 6 area		A1 × 0.5	A1 × 1.69
Peak 7 position (eV)			P1 + 9.75
Peak 7 area			A1 × 8.826

Table S2: Determined XPS fit parameters for each sample.

Species	P1 pos / eV	P1 area	P1 FWHM / eV	P2 FWHM / eV	P3 FWHM / eV	P4 FWHM / eV	P5 FWHM / eV	P6 FWHM / eV	P7 FWHM / eV	Weight
<b>Ni-AP</b>										
NiO	853.9	170.1	1	3.3	3.7	2	2.5			4 %
Ni(OH) <sub>2</sub>	854.8	1961.6	1.1	2.3	1.5	1.1	4.7	3		94 %
NiOOH	854.8	25	1.4	1.5	1.4	1.5	1.9	4	4.5	2 %
<b>Ni-100</b>										
NiO	853.9	585.3	1	3.3	3.7	2	2.5			17 %
Ni(OH) <sub>2</sub>	854.9	1492	1.1	2.3	1.5	1.1	4.7	3		83 %
NiOOH	854.8	0.6	1.4	1.5	1.4	1.5	1.9	4	4.5	0 %
<b>Ni-250</b>										
NiO	853.7	4171.2	1	3.3	3.7	2	2.5			79 %
Ni(OH) <sub>2</sub>	854.7	568.5	1.1	2.3	1.5	1.1	4.7	3		20 %
NiOOH	854.8	4	1.4	1.5	1.4	1.5	1.9	4	4.5	1 %
<b>Ni-300</b>										
NiO	853.6	5884.1	1	3.3	3.7	2	2.5			89 %
Ni(OH) <sub>2</sub>	854.7	303.8	1.1	2.3	1.5	1.1	4.7	3		9 %
NiOOH	854.8	57.4	1.4	1.5	1.4	1.5	1.9	4	4.5	2 %
<b>Ni-600</b>										
NiO	853.7	5291.9	1	3.3	3.7	2	2.5			95 %
Ni(OH) <sub>2</sub>	853.9	91.1	1.1	2.3	1.5	1.1	4.7	3		1 %
NiOOH	854.8	30	1.4	1.5	1.4	1.5	1.9	4	4.5	4 %

Table S3: EXAFS fit parameters for all samples.

Sample	$N$	$E_0 / \text{eV}$	$R_{\text{Ni-O}} / \text{\AA}$	$R_{\text{Ni-Ni}} / \text{\AA}$	$\sigma^2(\text{O}) / \text{\AA}^2$	$\sigma^2(\text{Ni}) / \text{\AA}^2$
<b>Ni-AP</b>	$4.7 \pm 0.4$	$-4 \pm 1$	$2.05 \pm 0.010$	$3.08 \pm 0.028$	$0.0067 \pm 0.001$	$0.033 \pm 0.004$
<b>Ni-100</b>	$4.4 \pm 0.6$	$-4 \pm 2$	$2.05 \pm 0.0010$	$3.06 \pm 0.018$	$0.007 \pm 0.001$	$0.024 \pm 0.002$
<b>Ni-200</b>	$4.8 \pm 0.8$	$-4 \pm 2$	$2.5 \pm 0.011$	$3.03 \pm 0.019$	$0.0084 \pm 0.002$	$0.024 \pm 0.002$
<b>Ni-230</b>	$4.4 \pm 0.5$	$-3 \pm 1$	$2.05 \pm 0.012$	$3.03 \pm 0.017$	$0.0068 \pm 0.002$	$0.020 \pm 0.002$
<b>Ni-250</b>	$5.6 \pm 0.8$	$-2 \pm 1$	$2.07 \pm 0.017$	$2.99 \pm 0.011$	$0.010 \pm 0.003$	$0.010 \pm 0.001$
<b>Ni-275</b>	$5.8 \pm 0.9$	$-2 \pm 1$	$2.08 \pm 0.017$	$2.99 \pm 0.012$	$0.009 \pm 0.003$	$0.010 \pm 0.002$
<b>Ni-300</b>	$5.6 \pm 0.5$	$-3 \pm 1$	$2.08 \pm 0.010$	$2.97 \pm 0.007$	$0.009 \pm 0.002$	$0.009 \pm 0.0008$
<b>Ni-400</b>	$5.7 \pm 0.4$	$-3 \pm 1$	$2.08 \pm 0.010$	$2.96 \pm 0.006$	$0.008 \pm 0.002$	$0.008 \pm 0.0007$
<b>Ni-500</b>	$6.0 \pm 0.4$	$-3 \pm 1$	$2.08 \pm 0.009$	$2.96 \pm 0.005$	$0.009 \pm 0.002$	$0.008 \pm 0.0007$
<b>Ni-600</b>	$5.9 \pm 0.5$	$-3 \pm 1$	$2.08 \pm 0.011$	$2.96 \pm 0.007$	$0.008 \pm 0.002$	$0.007 \pm 0.0008$
<b>Ni-AP-PO</b>	$4.3 \pm 0.8$	$-4 \pm 2$	$1.98 \pm 0.02$	$2.93 \pm 0.03$	$0.013 \pm 0.004$	$0.027 \pm 0.004$
<b>Ni-100-PO</b>	$4.2 \pm 0.6$	$-4 \pm 1$	$2.0 \pm 0.02$	$2.96 \pm 0.02$	$0.012 \pm 0.003$	$0.028 \pm 0.003$
<b>Ni-200-PO</b>	$4.1 \pm 0.3$	$-3 \pm 1$	$2.02 \pm 0.01$	$2.97 \pm 0.01$	$0.010 \pm 0.002$	$0.018 \pm 0.001$
<b>Ni-300-PO</b>	$4.7 \pm 0.3$	$-3 \pm 1$	$2.04 \pm 0.01$	$2.95 \pm 0.01$	$0.011 \pm 0.002$	$0.011 \pm 0.008$
<b>Ni-400-PO</b>	$5.1 \pm 0.4$	$-2 \pm 1$	$2.06 \pm 0.01$	$2.96 \pm 0.01$	$0.010 \pm 0.002$	$0.009 \pm 0.0008$
<b>Ni-500-PO</b>	$5.6 \pm 0.4$	$-3 \pm 1$	$2.07 \pm 0.01$	$2.96 \pm 0.01$	$0.008 \pm 0.002$	$0.008 \pm 0.0007$
<b>Ni-600-PO</b>	$5.4 \pm 0.4$	$-3 \pm 1$	$2.07 \pm 0.01$	$2.96 \pm 0.01$	$0.008 \pm 0.002$	$0.008 \pm 0.0008$

Table S4: Coloring rates  $r$  (in  $\text{s}^{-1}$ ) and coloration times  $\tau$  (in s) at different applied potentials  $E$ 

sample	$r$ ( $\tau$ )		
	$E = E_{\text{p,a}}$	$E = 1.9 \text{ V}$	$E = 2.4 \text{ V}$
<b>Ni-100<sup>a</sup></b>	0.3 (3.2)	1.7 (0.6)	2.5 (0.4)
<b>Ni-300<sup>b</sup></b>	0.2 (4.3)	1.4 (0.7)	2.0 (0.5)
<b>Ni-600<sup>c</sup></b>	0.5 (2.2)	3.3 (0.3)	5 (0.2)

<sup>a</sup>  $E_{\text{p,a}} = 1.38 \text{ V}$  vs RHE; <sup>b</sup>  $E_{\text{p,a}} = 1.33 \text{ V}$  vs RHE;<sup>c</sup>  $E_{\text{p,a}} = 1.28 \text{ V}$  vs RHE